ELSEVIER

Journal of Structural Geology 29 (2007) 1049–1069

JOURNAL OF STRUCTURAL GEOLOGY

www.elsevier.com/locate/jsg

Creep and strain-dependent microstructures of synthetic anorthite–diopside aggregates

A. Dimanov [a,*], E. Rybacki [b], R. Wirth [b], G. Dresen [b]

[a] *Laboratoire de Mécanique des Solides, UMR 7649, Ecole Polytechnique, Bat 65, Route de Saclay, 91128 Palaiseau, France*
[b] *GeoForschungsZentrum Potsdam, Telegrafenberg, 14473 Potsdam, Germany*

Received 4 May 2006; received in revised form 15 February 2007; accepted 18 February 2007
Available online 3 March 2007

Abstract

We investigated plastic deformation of fine-grained synthetic diopside and two-phase anorthite–diopside aggregates in triaxial compression and torsion (up to $\gamma \sim 5$). Temperature, confining pressure and stress ranged between 950–1180°C, 200–400 MPa and 5–500 MPa, respectively. Water content of samples ranged between $\sim 0.005 \pm 0.002$ and 0.075 ± 0.025 wt% H_2O. All samples deformed in linear-viscous creep with a stress exponent of 1.0 ± 0.2. The activation energy ranged between 571 ± 53 and 290 ± 28 kJ/mol, depending on mineralogy and water content. Sample strength depended on water fugacity with an exponent of 1.55 ± 0.25. Samples deformed in torsion and coaxial compression gave similar flow laws, in spite of significant differences in the corresponding microstructures. Scanning and transmission electron microscopy of two-phase samples deformed in torsion showed phase mixing, cavitation and dislocation processes. We suggest that linear-viscous creep of fine-grained two-phase aggregates involved grain boundary sliding accommodated by grain boundary diffusion and significant dislocation accommodation at high strains. We also observed that cavity coalescence and microcracking led to sample failure. Hence, dynamic instabilities may exist in high-strain shear zones accommodating viscous deformation in the lower continental crust.

Keywords: Lower crust; Shear zones; Two-phase rocks; Diffusion creep; High strain; Ductile failure

1. Introduction

Earthquake activity, structure and kinematics of large-scale faults transecting the brittle upper crust are strongly controlled by temperature- and pressure-varying viscosities of rocks at mid- to lower-crustal depth. Recent results from mechanical modelling suggest that the structural complexity of strike-slip fault systems and seismic recurrence intervals are significantly affected by viscous flow in the lower crust (Bourne, 2003; Rolandone et al., 2004; Savage, 2000). The time-averaged depths of seismic activity at major strike-slip faults transecting the continental crust such as the San Andreas Fault and the North Anatolian Fault Zone indicate a broad transition from brittle and/or friction-controlled deformation to aseismic creep at about 20 ± 5 km depth depending on local heat flow, shear strain rates and petrological composition (Hauksson, 2000; Magistrale and Zhou, 1996; Özalaybay et al., 2002; Tibi et al., 2001). However, slip-rate distribution and deformation mechanisms operating in fault zones at mid- to lower-crustal depth are complex and may vary considerably in space and time (Bürgmann et al., 2002; Tse and Rice, 1986). For example, time-dependent shallowing of aftershock activity as observed for the 1992 Landers earthquake is attributed to increasing contribution of viscous creep at the expense of brittle deformation (Rolandone et al., 2004). Recently, studies of mylonite shear zones exhumed from the base of the seismogenic upper crust reveal microstructures associated with high-stress episodes during coseismic loading overprinted by microstructures due to low-stress plastic flow that reflect post-seismic stress relaxation (Ellis and Stöckhert, 2004; Trepmann and Stöckhert, 2003). Analytical modelling indicates that

* Corresponding author. Fax: +33 1 96 33 30 28.
E-mail address: dimanov@lms.polytechnique.fr (A. Dimanov).

0191-8141/$ - see front matter © 2007 Elsevier Ltd. All rights reserved.
doi:10.1016/j.jsg.2007.02.010

coseismic stress pulses likely scale with stress drops and decay rapidly with distance from earthquake hypocenters (Montési, 2004).

The complex spatio-temporal variation of stress and slip-rate at crustal depth is still inaccessible to direct observations but may be constrained by a combination of laboratory studies of rheology, field observations and modelling of active deformation. Geodetic records of postseismic surface deformation at strike-slip faults span just a few years to decades, but existing data generally indicate that earthquake-induced perturbations of strain rates and stresses decay on timescales of <1 to 100 years (Hearn et al., 2002; Kenner and Segall, 2000, 2003; Savage and Svarc, 1997; Savage et al., 2003). Estimates of ''long-term'' relaxation times are on the order of a few decades, suggesting that creep viscosities in the lower crust and upper mantle are of the order of 10^{18}–10^{20} Pa.s (Hetland and Hager, 2003; Kenner and Segall, 2000; Li and Rice, 1987; Thatcher, 1983).

Field studies of exposed sections from the base of the seismogenic crust often show deformation localized into high-strain shear zones containing fine-grained (<50 μm) ultramylonites. Partly, these zones may represent the downward continuation of seismogenic faults transecting the brittle upper crust (Scholz, 1990; Sibson, 1977). Shear zones cutting through the lower crust often contain fine-grained mixtures of dominantly feldspar, pyroxene and amphibole assumed to deform by linear-viscous flow (Allison et al., 1979; Behrmann and Mainprice, 1987; Egydio-Silva et al., 2002; Kenkmann and Dresen, 1998, 2002; Kruse and Stünitz, 1999; Steffen et al., 2001).

However, to infer bulk mechanical behaviour from local microstructure observations is a daunting task. For example, microstructural criteria commonly used to infer grain size-sensitive, potentially superplastic flow in shear zone mylonites include a small and equant grain size, phase mixing, low dislocation densities and cavitation (Behrmann, 1985; Boullier and Gueguen, 1975). However, even very fine-grained ultramylonite rocks often show evidence for non-linear creep, such as elevated dislocation densities, dynamic recrystallization and crystallographic textures (Behrmann and Mainprice, 1987; Kenkmann and Dresen, 2002). In fact, similar to ceramic materials, grain size-sensitive flow and grain boundary sliding in rocks often involve multiple accommodation mechanisms that are not yet fully understood (Nieh et al., 1997; Paterson, 1990; Wakai et al., 1999; Zelin and Mukherjee, 1996).

Laboratory studies provide independent constraints on viscosities and deformation mechanisms dominating high-temperature creep in the lower crust and mantle. However, available experimental data for rocks typical of the lower crust are still scarce. In particular, there are only a few studies on fine-grained rocks deforming at low stresses (Bystricky and Mackwell, 2001; Dimanov et al., 2003; Mackwell et al., 1998). Robust flow laws now exist for dislocation and diffusion-controlled creep of feldspar rocks (Dimanov et al., 1998; Rybacki and Dresen, 2000, 2004; Rybacki et al., 2004) and clinopyroxene rocks (Dimanov and Dresen, 2005). Recently, Dimanov and Dresen (2005) studied the high-temperature creep strength of anorthite–diopside mixtures exploring the effect of mineralogical composition on the constitutive behaviour.

In this paper we investigate the mechanical behaviour and microstructure evolution of synthetic feldspar–pyroxene aggregates to high strains. We discuss the role of phase mixing and cavitation and present the first experimental results on failure of rocks by cavitation during ductile flow at high temperatures and pressures. The synthetic rocks serve as analogues for fine-grained ultramylonites frequently found in shear zones transecting mafic rock assemblages in the lower crust.

2. Experimental procedures

2.1. Starting materials and sample preparation

We performed deformation experiments on 10 synthetic two-phase plagioclase–clinopyroxene aggregates containing 50 vol% anorthite and 50 vol% diopside and two synthetic single-phase clinopyroxene aggregates. Samples were prepared from glass powders of anorthite and diopside provided by Schott Glasswerk (particle size $d < 40$ μm, <1 wt% impurities). The powders were mechanically mixed in an agate mortar in alcohol. The mixtures were oven dried over a week and then cold-pressed in cylindrical steel cans 2 cm in height and 1 cm or 1.5 cm in diameter for axial and torsion tests, respectively. One cold-pressed two-phase specimen was pre-dried at 850°C and 0.1 MPa in a CO/CO_2 atmosphere for 3 days. As-received or pre-dried cold-pressed specimens were hot-isostatically pressed (HIPed) at 300 MPa and 1100°C for 2–5 h (for details see Wang et al., 1996; Dimanov et al., 1999; Rybacki and Dresen, 2000). During HIP, the fine-grained glass powder crystallized to form dense fine-grained mixtures of anorthite and diopside or pure diopside. For axial compression experiments, samples were deformed directly after HIPing. Sample dimensions of HIPed samples show good reproducibility with 16.5 ± 1.0 mm length and 8.00 ± 0.50 mm diameter (see also Dimanov et al., 2003). The diameter for a single specimen was constant within ±0.2 mm except very close to the end spacers. Specimens deformed in torsion were precision-ground from the larger size HIPed samples to produce cylinders 10 mm in diameter and 7 mm in length.

2.2. Microstructures and water content of hot-isostatically pressed samples

Microstructures of undeformed and deformed samples were investigated using a scanning electron microscope (SEM; Zeiss DSM 962) and transmission electron microscope (TEM, Phillips CM 200). Appropriate sections were cut parallel and perpendicular to the sample axis. Thick sections prepared for SEM observations were polished and etched thermally to reveal grain boundaries. Thin foils for TEM observations were prepared by ion thinning thin sections from otherwise untreated deformed material.

Thick sections of hot-pressed specimens were ground and polished to a 0.3 μm finish. To reveal grain boundaries, samples were thermally etched for 24 h at 1423 K at atmospheric pressure. Grain sizes and grain size distribution were determined with the linear intercept method from SEM micrographs. Arithmetic mean intercept length was converted to average grain size using correction factors of 1.9 and 1.78 for anorthite and diopside, respectively, to account for the difference in grain shape (Dimanov et al., 2003). Undeformed two-phase samples show clusters of diopside and anorthite grains (Fig. 1a and b). The clusters correspond to the size of the initial glass particles. We determined arithmetic grain size of anorthite and diopside within clusters of $d_{An} = 3.8 \pm 0.5$ μm and $d_{Di} = 2.3 \pm 0.4$ μm, respectively (Dimanov et al., 2003). Grain size in pure diopside samples is slightly larger than in two-phase materials: $d_{Di} = 2.5 \pm 0.5$ μm (Fig. 1c). Grain growth in pure diopside and two-phase materials during experiments was insignificant, suggesting that grain size was effectively pinned by second phases and pores (Olgaard and Evans, 1988). We did not observe obvious microstructural differences between the pre-dried and as-received two-phase samples. Porosity of samples was estimated <1% using Archimedes method and immersion in water and alcohol. TEM micrographs of undeformed samples show equant diopside grains with 120° triple junctions and elongated anorthite grains with numerous growth twins (Fig. 2a). Dislocation densities in diopside and anorthite (Fig. 2) are low ($\rho < 10^{11}$ m^{-2}). Numerous fluid inclusions are present. They evidence the adsorbed water during powder processing. A few residual glass pockets were observed at multiple grain junctions (Fig. 2b), but grain boundaries appear free of glass in high-resolution TEM to a resolution of <1 nm (Fig. 3). Glass content is estimated <1 vol%.

Fourier-transformed infrared spectroscopy (FTIR) was used to quantify the water content of hot-pressed and deformed samples (Rybacki and Dresen, 2000; Dimanov et al., 1999, 2003; Dimanov and Dresen, 2005; Rybacki et al., 2006). The spectrometer (Bruker IFS-66v) is equipped with a microscope with minimum spot size of about 60 μm. Line scans oriented parallel and perpendicular to the long specimen axis indicate that the water content is homogeneous on the sample scale. For quantitative estimates of water content of the two-phase aggregates Beer–Lambert's law was used with volume-weighted average molar absorptivities for plagioclase (Beran, 1987) and diopside (Bell et al., 1995). The starting glass powders are highly hygroscopic adsorbing significant quantities of water. As is, "wet" specimens contain bulk trace amounts of water of ~0.075 ± 0.025 wt%. Similar water contents as for the wet specimens were reported from natural gabbroic ultramylonites (Kenkmann, 1997). A typical FTIR spectrum is shown in Fig. 4. A broad absorption band indicating molecular water may partly be accounted for by numerous small fluid inclusions observed in TEM (Fig. 2). In plagioclase, a broad absorption band may also result from hydroxyl groups (OH^-) and water-related point defects (Beran, 1986, 1987; Johnson and Rossman, 2004). A sharp peak centred at wave number 3646 cm^{-1} indicates structurally bonded hydroxyl groups in diopside (Wilkins and Sabine, 1973; Beran, 1976; Ingrin et al., 1989; Skogby and Rossman, 1989; Bell et al., 1995). Recent studies of hydrogen solubility in natural diopside at high pressure (500 MPa) and temperature (1273–1373 K) (Bromiley et al., 2004) suggest that at our experimental conditions (200–400 MPa and 1323–1523 K) as-is (wet) samples

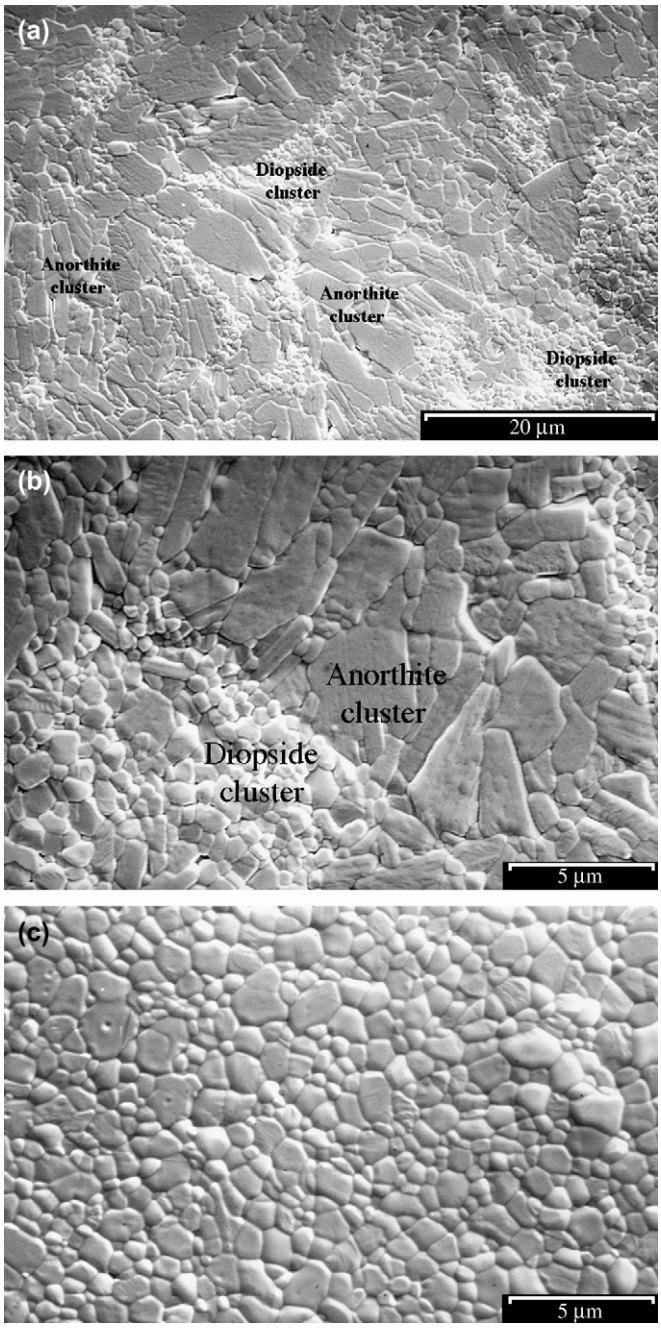

Fig. 1. SEM micrographs from the starting materials. (a) Overview showing the characteristic "single-phase clusters," resulting from the crystallization of glass particles, which are much larger than the actual grain size. (b) Close-up at the boundary between diopside and anorthite clusters. Diopside grains are equant, whilst anorthite grains are elongated and lath shaped. Grain size distribution is unimodal in both phases. (c) Close-up of diopside single-phase sample. Grain size is slightly larger than in diopside clusters in two-phase materials. Grain size distribution is unimodal.

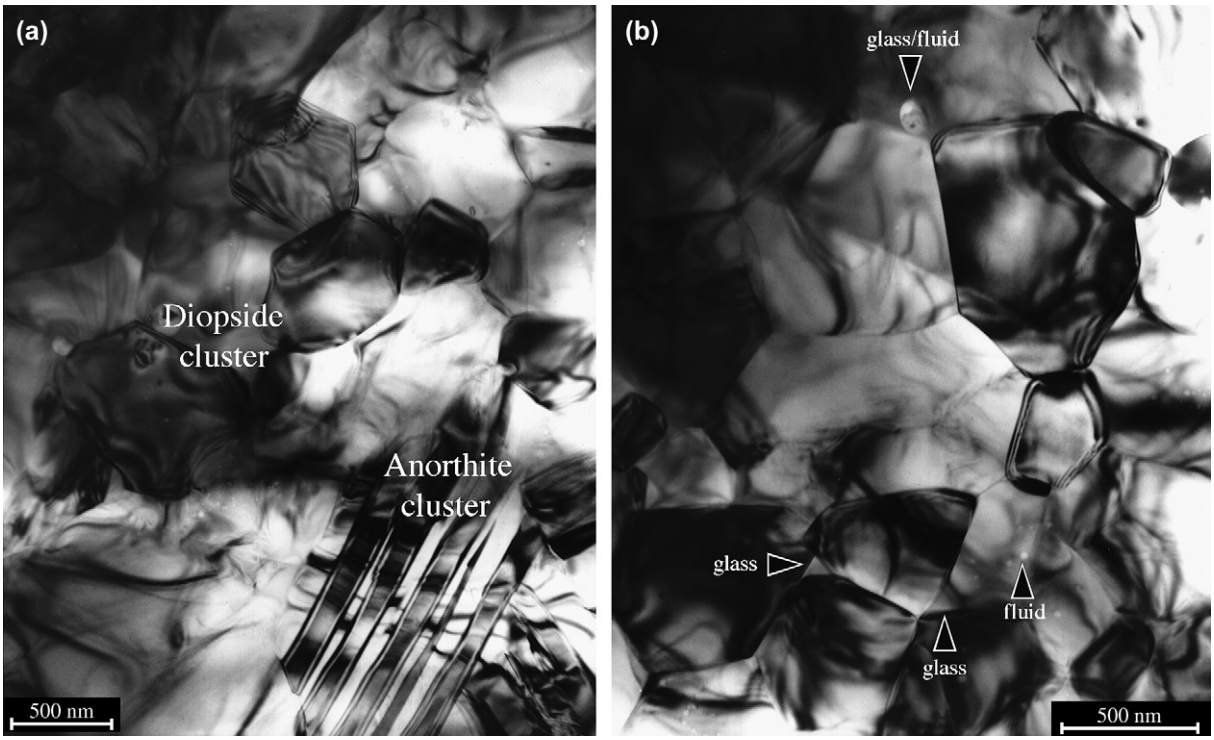

Fig. 2. TEM micrographs from the wet starting material. (a) Overview showing the interphase region between two ''single-phases clusters''. The anorthite is characterized by lath-shaped grains and growth twins. Diopside grains are equant. Dislocation densities are low. (b) Close-up of a diopside cluster. Arrows indicate residual glass pockets, intracrystalline fluid inclusions and inclusions in residual glass pockets.

may be considered water-saturated. Although some diffusive dehydration may be expected in the gas apparatus, FTIR measurements of as-is hot-pressed and deformed samples do not show evidence of significant water loss during deformation runs of up to 2 days (Rybacki and Dresen, 2000; Dimanov et al., 2003; Dimanov and Dresen, 2005). Small peaks at around 2900 cm^{-1} are likely due to C–H stretching motions. Carbon impurities might diffuse from the steel jackets into

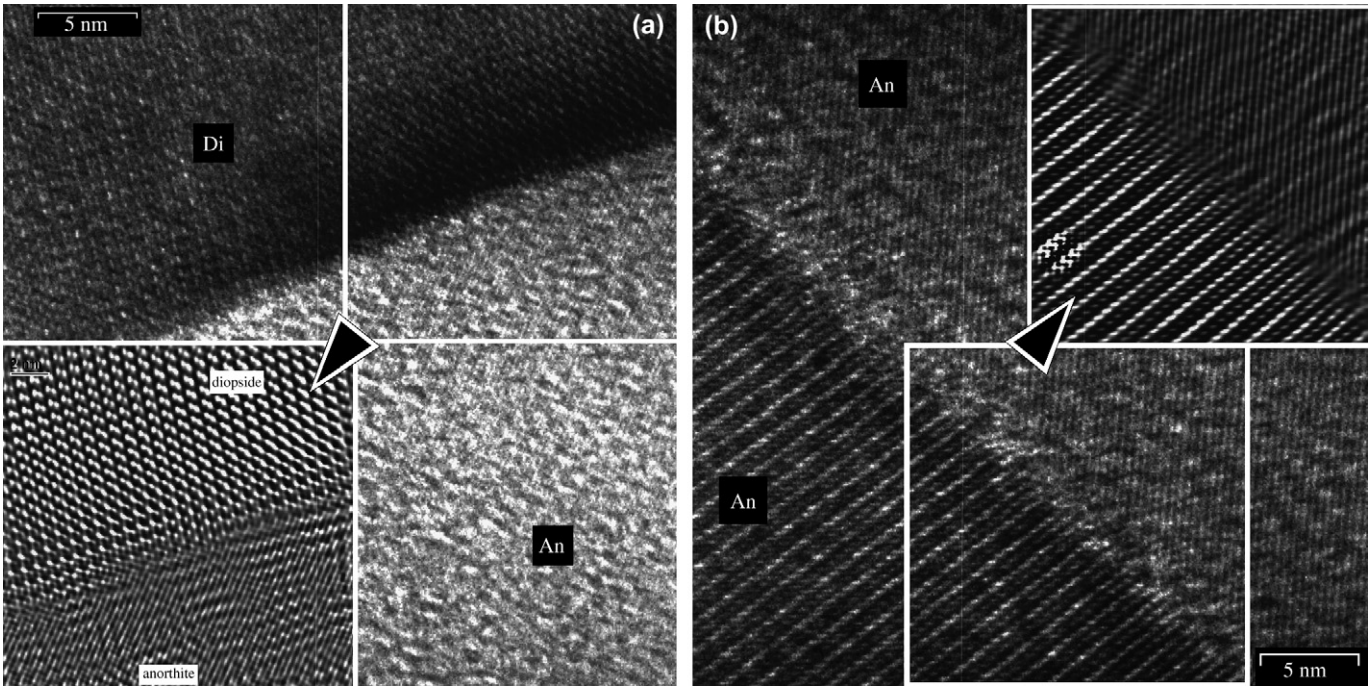

Fig. 3. High-resolution TEM micrographs from the wet starting material. Crystal lattice fringe and Fourier Transform Filtered images of grain boundary areas (arrows) show that two-grain contacts are free of amorphous material. (a) Anorthite–diopside interphase boundary. (b) Anorthite grain boundary.

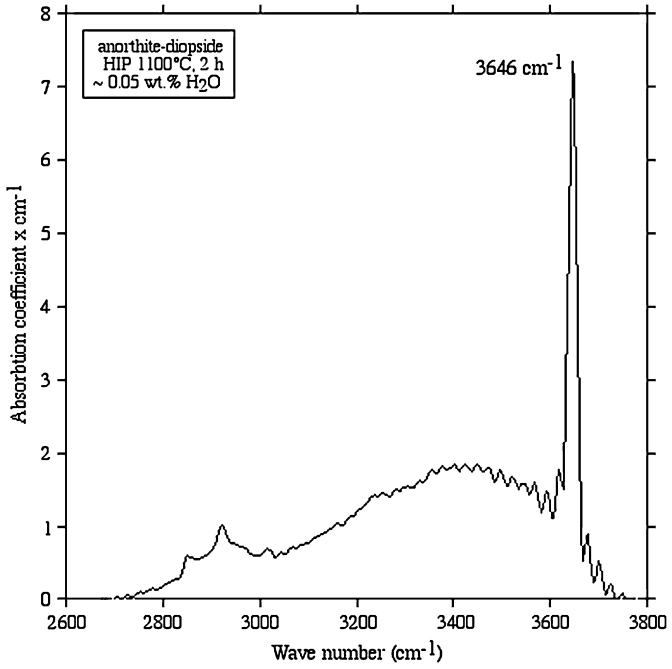

Fig. 4. Smoothed and base-line corrected FTIR spectrum of the starting wet material. The spike at 3646 cm^{-1} is characteristic of hydroxyl groups. The broad band represents molecular water. The small spikes around 2900 cm^{-1} are due to C–H vibrations. Small amount of C is present in the sample due to contamination from the steel jacket.

the samples during hot pressing. For instance, hot-pressed samples are greyish, but become white after annealing in air. Since the FTIR spot size significantly exceeds the grain size, the estimated water content refers to grains and grain boundaries. The pre-dried sample has $\sim$0.005 $\pm$ 0.002 wt% H_2O and is considered "nominally dry" (Dimanov et al., 1999; Rybacki and Dresen, 2000; Dimanov and Dresen, 2005; Rybacki et al., 2006).

2.3. Deformation experiments

Deformation experiments were performed in a Paterson-type gas medium apparatus in triaxial compression and torsion testing between 200 MPa and 400 MPa confining pressure, temperatures between $T = 950–1180$°C and differential stresses ranging from $\sigma = 5–500$ MPa. Samples were contained in steel sleeves between alumina spacers and partially stabilized zirconia end-pistons.

Axial compression tests were performed on one sample in constant strain rate and on nine different specimens as a series of stress and temperature-stepping creep tests (Table 1). Differential stresses varied between about 15 MPa to about 500 MPa resulting in strain rates between about 3×10^{-7} s^{-1} to about 1.5×10^{-4} s^{-1}. Raw data were corrected for the strength of the steel jackets and for sample distortion assuming constant volume (Rybacki and Dresen, 2000). Confining pressure was either 200 MPa or 300 MPa. For single steps the load was maintained constant within $\pm$0.02 kN resulting in a variation of axial stress of $<$1 MPa. Displacement was measured using a linear-variable displacement transducer (LVDT) with an accuracy of 2 μm. Temperature was monitored using a Pt/Pt–10%Rh thermocouple within 5 mm of the specimen top end. The temperature gradient along the sample axis was $<$5 K. Samples are deformed following hot pressing. The uncertainties in differential stress and strain rate, related to load cell sensitivity, jacket strength corrections, minor sample bulging and slight variations in sample dimensions are $<$5% (Dimanov and Dresen, 2005). Temperature uncertainty is less than 0.5%. All samples were cooled under load at a rate of 40 K/min.

Large-strain torsion experiments were performed on three individual samples at $P = 400$ MPa. The experiments were performed at constant twist rate. Twist rate and temperature were varied stepwise as was temperature to estimate flow law parameters. We achieved maximum shear strains for individual samples of about $\gamma \sim 5$. The torque–twist data were corrected for jacket strength, apparatus compliance and for zero-torque offsets (Rybacki et al., 2003). Calculation of maximum shear stress and shear strain at the sample periphery from torque and twist data follows Paterson and Olgaard (2000). Uncertainties in shear stress due to the torque cell and jacket strength corrections are less than 2 MPa.

3. Results

3.1. Mechanical data

The mechanical data set for axial deformation experiments are given in Table 1. For individual axial creep steps, strains were about 3% with a total strain of up to 28% for a single specimen. Secondary creep approximating steady state was reached at about 0.5–1% axial strain. However, in opposition to samples deformed axially in creep tests, samples deformed axially in constant strain rate steps did not fully reach steady state within 3%. Moderate work hardening (from 130 MPa to 180 MPa flow stress) was also observed between 12% and 26% (maximum strain) for a two-phase sample (ADSW00-b) deformed in a single step at 1100°C and 1.2×10^{-4} s^{-1}. The data in Table 1 report the maximum flow stress corresponding to the maximum strain at each step.

The mechanical data set for torsion experiments are given in Table 2. Fig. 5 shows the experimental curves of flow stress versus shear strain. For the first two samples we varied both twist rate and temperature to obtain the flow stress exponent n and the activation energy Q for deformation at different shear strains. Within error bars both parameters remain almost similar independent of strain in the range of $\gamma \sim 0.2$ to $\gamma \sim 4.5$. During the second temperature step sample ADSW2 failed unstably at a shear strain of $\gamma \sim 4.3$, producing a macroscopic shear fracture that cut across the entire sample (Fig. 5b). The initial strain hardening is important up to about $\gamma \sim 1$ for all of the three samples. Two samples present further moderate strengthening up to shear strain of $\gamma \sim 2$. At higher strains these samples show nearly steady state up to $\gamma \sim 4–5$ (Fig. 5a and b). The third sample shows an apparent

Table 1
Experimental data for coaxial deformation of synthetic two-phase anorthite–diopside aggregates for dry (ADSD) or wet (ADSW) conditions and synthetic diopside aggregates (DSW) for wet conditions

P (MPa)	T (°C)	log σ (MPa)	log dϵ/dt (s^{-1})
ADSD01-a			
300	1100	1.602	−5.122
300	1100	1.176	−5.467
300	1100	1.431	−5.278
300	1100	1.681	−4.936
300	1100	1.839	−4.757
300	1100	2.000	−4.590
300	1100	2.146	−4.431
300	1150	1.217	−4.830
300	1150	1.447	−4.569
300	1150	1.602	−4.424
300	1150	1.699	−4.358
300	1150	1.785	−4.276
300	1150	1.903	−4.148
300	1050	1.322	−6.223
300	1050	1.58	−6.207
300	1050	1.914	−5.777
300	1050	2.086	−5.575
300	1050	2.201	−5.479
300	1050	2.386	−5.228
300	1050	2.547	−4.943
300	1050	2.704	−4.701
ADSW00-b			
300	1100	2.255	−3.916
ADSW01-b			
300	1100	1.568	−4.500
300	1100	1.892	−4.204
300	1100	2.169	−3.859
300	1100	1.556	−4.754
300	1050	1.889	−4.701
300	1050	2.241	−4.380
ADSW02-b			
200	1100	1.653	−4.440
200	1100	2.000	−4.138
200	1100	2.334	−3.827
200	1050	2.033	−4.642
200	1050	2.403	−4.353
ADSW01-a			
300	1100	1.204	−4.883
300	1100	1.505	−4.556
300	1100	1.602	−4.383
300	1100	1.792	−4.159
300	1050	1.176	−5.462
300	1050	1.580	−5.017
300	1050	1.778	−4.747
300	1050	1.959	−4.519
300	1050	2.149	−4.310
300	1000	1.699	−5.463
300	1000	1.845	−5.220
300	1000	1.954	−5.116
300	1000	2.083	−4.959
300	1000	2.204	−4.827
300	950	1.301	−6.611
300	950	1.778	−5.959
300	950	1.954	−5.674
300	950	2.146	−5.553
300	950	2.301	−5.299
300	950	2.401	−5.338
ADSW04-a			
300	1050	1.505	−4.983
300	1050	1.699	−4.741
300	1050	1.833	−4.581
300	1050	1.934	−4.494
300	1050	2.083	−4.344
300	1050	2.193	−4.237
300	1050	2.276	−4.148
300	1050	2.346	−4.064
300	1100	1.176	−4.883
300	1100	1.398	−4.623
300	1100	1.544	−4.447
300	1100	1.740	−4.212
300	1100	1.869	−4.069
300	1100	1.968	−3.958
300	1100	2.049	−3.892
ADSW03-a			
200	1100	1.987	−4.017
200	1100	1.568	−4.618
200	1100	1.161	−5.069
200	1100	1.415	−4.780
200	1100	1.568	−4.595
200	1100	1.760	−4.383
200	1100	1.886	−4.293
200	1100	1.982	−4.188
200	1100	2.068	−4.127
200	1050	1.580	−5.312
200	1050	1.763	−5.027
200	1050	1.889	−4.936
200	1050	1.991	−4.785
200	1050	2.068	−4.712
200	1050	2.167	−4.583
200	1050	2.246	−4.544
200	1050	2.333	−4.476
200	1050	2.408	−4.403
DSW01-b			
300	1100	2.074	−3.742
DSW02-a			
300	1100	1.282	−4.883
300	1100	0.869	−4.556
300	1100	1.093	−4.383
300	1100	1.281	−4.159
300	1100	1.389	−5.462
300	1100	1.471	−5.017
300	1000	1.571	−4.747
300	1000	1.774	−4.519
300	1000	1.422	−4.310
300	1000	1.900	−5.463
300	1000	2.079	−5.220
300	900	1.997	−5.553
300	900	1.250	−5.299
300	900	1.780	−5.338

Extensions -a and -b indicate creep tests and constant strain rate tests, respectively.

steady state between $\gamma \sim 1$ and $\gamma \sim 3$, with a moderate strengthening at higher strain (Fig. 5c). The torsion data are compared to the results from axial compression testing by converting shear stress τ and shear strain rate dγ/dt to equivalent axial stress σ and equivalent axial strain rate dϵ/dt, respectively (Paterson and Olgaard, 2000):

Table 2
Experimental data for torsion deformation of synthetic two-phase anorthite–diopside aggregates for wet conditions

P (MPa)	T (°C)	log σ (MPa)	log dϵ/dt (s^{-1})
ADSWT1			
$\gamma \sim 0.1$			
400	1150	1.450	−3.830
400	1150	0.978	−4.321
400	1150	0.444	−4.675
$\gamma \sim 0.3$			
400	1150	1.550	−3.812
400	1150	1.031	−4.306
400	1150	0.601	−4.663
$\gamma \sim 1.2$			
400	1150	1.676	−3.776
400	1120	1.943	−3.776
400	1180	1.304	−3.776
$\gamma \sim 2.1$			
400	1150	1.757	−3.767
400	1150	1.188	−4.268
400	1150	0.944	−4.634
$\gamma \sim 3.9$			
400	1150	1.798	−3.772
400	1120	2.051	−3.772
400	1180	1.357	−3.772
$\gamma \sim 4.4$			
400	1150	1.811	−3.767
400	1150	1.112	−4.284
400	1150	0.694	−4.597
ADSWT2			
$\gamma \sim 0.2$			
400	1100	1.779	−3.925
400	1100	1.449	−4.275
400	1100	1.051	−4.629
$\gamma \sim 0.5$			
400	1100	1.850	−3.909
400	1100	1.480	−4.241
400	1100	1.212	−4.598
$\gamma \sim 1.2$			
400	1100	1.885	−3.910
400	1080	2.094	−3.910
400	1120	1.737	−3.910
$\gamma \sim 3.6$			
400	1100	1.956	−3.928
400	1100	1.503	−4.278
400	1100	1.254	−4.642
$\gamma \sim 4.2$			
400	1100	1.977	−3.910
400	1130	1.663	−3.910
400	1070	2.295	−3.910
ADSWT3			
$\gamma \sim 0.5$			
400	1150	1.678	−3.775
$\gamma \sim 2$			
400	1150	1.757	−3.775
$\gamma \sim 3.7$			
400	1150	1.755	−3.773
400	1150	1.383	−4.008
400	1150	0.998	−4.269
400	1150	0.481	−4.616
$\gamma \sim 4.5$			
400	1150	1.837	−3.776

Shear stress and shear strain rate are converted to equivalent axial stress and strain rate, respectively (see the text).

$$d\epsilon/dt = (d\gamma/dt)/3^{1/2} \quad (1)$$

$$\sigma = 3^{1/2}\tau$$

All measured data are fit to a power-law equation of the form:

$$\frac{d\epsilon}{dt} = A f_{H_2O}^{p} \sigma^{n} d^{-m} e^{-\frac{Q+PV}{RT}} \quad (2)$$

where p is the water fugacity exponent, n is the stress exponent, σ is the flow stress in MPa, dϵ/dt is the strain rate in s^{-1}, m is the grain size exponent, d is the grain size in μm, Q is the activation energy in kJ/mol, P is the confining pressure in GPa, and V is the activation volume in cm^3 mol^{-1}. R is the gas constant T is the absolute temperature and A is a material parameter in $MPa^{-(p+n)}$ μm^{-m} s^{-1}. The constitutive equations for high-temperature creep of hydrous diopside and dry and hydrous anorthite–diopside aggregates in axial compression are given in Table 3. The flow law obtained in torsion tests is given in Table 4.

3.1.1. Stress sensitivity in triaxial compression tests

Deformation in axial compression of wet diopside and both dry and wet anorthite–diopside aggregates is accommodated dominantly by linear-viscous (Newtonian) creep with $n \approx 1$ in the range of investigated temperatures (900–1150°C), pressures (200–300 MPa) and flow stresses (15–500 MPa). Stress exponents are between $n = 1.0 \pm 0.1$ and 1.3 ± 0.1 (Figs. 6, 7 and 9) as determined from constant strain rate tests and creep tests. Data from constant strain rate tests and creep tests are in good agreement (Figs. 6b, 7a and 9a).

At a confining pressure of 300 MPa and at 1050°C, the viscosity of the nominally dry sample is about one order of magnitude higher than that of hydrous specimens containing trace amounts of water (Fig. 6a and b).

For comparison with our diopside data (Fig. 7a) we have included data for diopside aggregates prepared from crushed natural single crystals of Dimanov and Dresen (2005) and data for aggregates prepared from crushed natural clinopyroxenite of Hier-Majumder et al. (2005). The original data from Hier-Majumder et al. (2005) and from Dimanov and Dresen (2005) correspond to grain boundary diffusion-controlled Newtonian flow, with mean grain sizes of ~14 μm and ~10 μm, respectively. These data were corrected for the differences in grain size with a grain size exponent $m = 3$. Our data closely agree with the data from Dimanov and Dresen (2005), but the samples from Hier-Majumder et al. (2005)

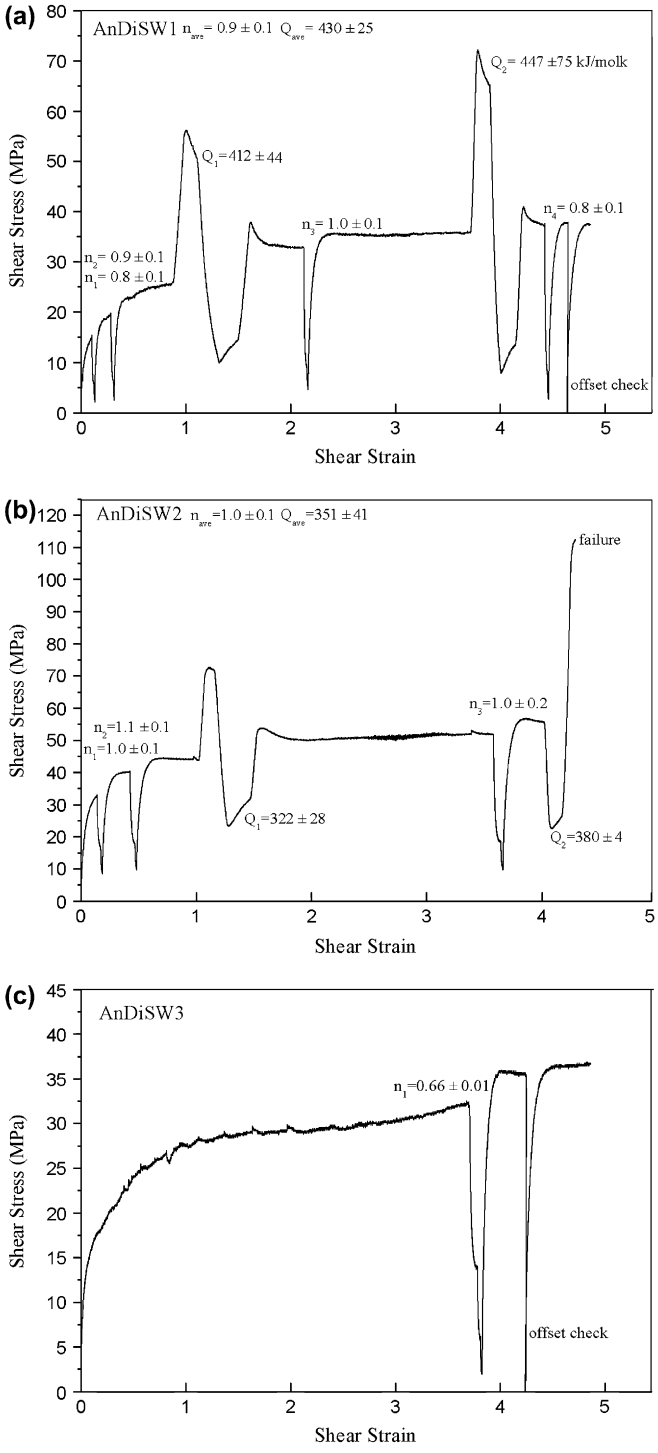

Fig. 5. Shear strain–shear stress plots of wet samples deformed in torsion. Strain rate- and temperature stepping were performed at different shear strains. The corresponding stress exponents, n, and activation energies, Q, are reported. (a) Shear stress–shear strain curve from sample AnDiSW1 deformed at constant shear strain rate $d\gamma/dt \sim 2.75 \times 10^{-4}$ s^{-1}. The flow stress is nearly constant after $\gamma \sim 1.5$. At the end of the experiment an offset check was performed. (b) Shear stress–shear strain curve from sample AnDiSW2 deformed at constant shear strain rate $d\gamma/dt \sim 2.2 \times 10^{-4}$ s^{-1}. The flow stress is nearly constant after $\gamma \sim 0.5$. The sample failed after the second step in temperature. (c) Shear stress–shear strain curve from sample AnDiSW3 deformed at constant shear strain rate $d\gamma/dt \sim 2.75 \times 10^{-4}$ s^{-1}. The flow stress is nearly constant between $\gamma \sim 1$ and 2.5, but increases slightly at higher strain. At the end of the experiment an offset check was performed.

are about an order of magnitude weaker than our samples. This discrepancy may be related to a different chemical composition of the starting materials. The clinopyroxenite used by Hier-Majumder et al. (2005) contains significantly more iron than the clinopyroxene crystals used by Dimanov and Dresen (2005).

In Fig. 7b we compare the two-phase data with data for anorthite–diopside aggregates from (Dimanov and Dresen, 2005) that contain 50 vol% glass-derived anorthite and 50 vol% diopside produced from crushed single crystals. Also shown is a comparison of our pure diopside data with results for pure diopside aggregates prepared from crushed natural diopside (Dimanov and Dresen, 2005). The wet diopside and two-phase aggregates from this study, produced from glass, are weaker than the corresponding diopside samples and anorthite–diopside mixtures containing crushed diopside single crystal fragments. This difference is likely due to the average grain size of the glass-derived diopside particles that is significantly smaller than in the samples of Dimanov and Dresen (2005). For comparison, we also show data for pure anorthite made from the same glass as used in this study (Rybacki and Dresen, 2000; Dimanov and Dresen, 2005).

3.1.2. Stress sensitivity in triaxial torsion tests

Three anorthite–diopside samples were tested in torsion at constant twist rate. Two samples were tested at 1150°C and one sample at 1100°C. Stress exponent and activation energy were determined by performing twist rate and temperature steps (Fig. 5). The twist rate steps produced maximum strain rates between 1.6×10^{-5} s^{-1} and 2.1×10^{-4} s^{-1}. Temperature steps were ±20°C and ±30°C above and below run temperature, thus covering the range 1070–1180°C. The data show good agreement between tests performed on the different samples. Stress exponents estimated from twist rate stepping at different shear strains ranged between $n = 0.7 \pm 0.1$ and 1.1 ± 0.1 for all of the three samples (Fig. 8). This observation suggests that the same deformation mechanism operates at low and at high strain.

3.1.3. Water fugacity sensitivity

The wet samples contain numerous fluid inclusions. Recent estimates of water solubility in diopside (Bromiley et al., 2004) suggest that our samples were water saturated at run conditions. Therefore we assume that water activity is ~1 and that fluid pressure approximates the confining pressure. The creep rate of hydrous anorthite–diopside aggregates increases significantly (by 50–100%, depending on temperature) with increasing confining pressure from 200 MPa to 300 MPa (Fig. 9a). Figs. 6, 8 and 9 show that the stress sensitivity is similar in compression and in torsion tests. The stress exponent does not depend on either confining pressure or finite strain (Figs. 8 and 9). These observations suggest that similar mechanisms dominate deformation of the samples tested in compression and in torsion. Therefore, we plot the entire data set for wet specimens deformed in torsion and axial compression versus water fugacity (Fig. 9b). Water fugacities

Table 3
Flow laws ($d\epsilon/dt = B\sigma\, e^{-Q/RT}$, where $B = Af_{H_2O}{}^p d^{-m}$) for wet and dry materials (labeled by W and D, respectively) in coaxial deformation at 300 MPa confining pressure

Material	B ($Pa^{-n}s^{-1}$)	n	Q (kJ/mol)
$An_{3.8}Di_{2.3}D$	$1.002 \times 10^{9\ +1.003\times10^{11}}_{\ -9.924\times10^{8}}$	1	571±53
$Di_{2.5}W$	$1.1455 \times 10^{-1\ +1.5018}_{\ -1.0643\times10^{-1}}$	1	290±28
$An_{3.8}Di_{2.3}W$	$6.6222 \times 10^{\ +6.1334\times10^{3}}_{\ -6.5514\times10}$	1	363±49

Grain size is given by the subscript to the phase.

were estimated from confining pressures at the experimental temperature according to Grevel and Chatterjee (1992). Strain rates for the two-phase mixtures were recalculated to account for the effect of confining pressure using an activation volume $V = 19$ cm^3 mol, which is a volume-weighted average of the data for anorthite ($V_{An} = 24 \pm 21$ cm^3 mol^{-1}, Rybacki et al., 2006) and diopside ($V_{Di} = 14 \pm 6$ cm^3 mol^{-1}, Hier-Majumder et al., 2005). At $T = 1100$°C, the data normalized for pressure yield a fugacity exponent $p = 1.55 \pm 0.25$. This value is similar to values obtained for the pure phases ($p_{An} = 1.0 \pm 0.3$, Rybacki et al., 2006 and $p_{Di} = 1.4 \pm 0.2$, Hier-Majumder et al., 2005) and other silicates such as quartz ($p_{Qtz} = 1-2$, Gleason and Tullis, 1995; Kohlstedt et al., 1995; Post et al., 1996; Hirth et al., 2001) and olivine ($p_{Ol} = 0.7-1.25$, Mei and Kohlstedt, 2000a,b; Karato and Jung, 2003).

3.1.4. Activation energy

In Fig. 10 we have compiled our data in Arrhenius diagrams (log strain rate versus inverse absolute temperature) and we compare them to previously reported data of linear-viscous flow of diopside (Fig. 10a) and anorthite–diopside samples (Fig. 10b). All data were recalculated to a common flow stress of 10 MPa using a stress exponent $n = 1$. The grain size of diopside samples studied by Dimanov and Dresen (2005) is <25 μm with a mean grain size of about 10 μm, similar to the clinopyroxenite grain size used by Hier-Majumder et al. (2005). These data were recalculated to a grain size of 2.5 μm using a grain size exponent $m = 3$, reported in the former studies. Wet diopside aggregates prepared from glass have a creep activation energy of $Q = 290 \pm 28$ kJ/mol (Fig. 10a), which is consistent with the values reported by Dimanov and Dresen (2005) and Hier-Majumder et al. (2005) for diopside aggregates prepared from natural diopside single crystal and natural diopsidite, respectively. However, the iron-rich samples of Hier-Majumder et al. (2005) are substantially weaker than the iron-poor (Dimanov and Dresen, 2005) and the iron-free (present study) samples. The different pre-exponential

Table 4
Flow laws ($d\epsilon/dt = B\sigma\, e^{-Q/RT}$, where $B = Af_{H2O}{}^p d^{-m}$) for wet materials in torsion deformation at 400 MPa confining pressure

Material	B ($Pa^{-n}s^{-1}$)	n	Q (kJ/mol)
$An_{3.8}Di_{2.3}W$	$2.0464^{+5.0322\times10^{2}}_{-2.0399}$	1	319 ± 64

Grain size is given by the subscript to the phase. Shear stress and shear strain rate are converted to equivalent axial stress and strain rate, respectively (see the text).

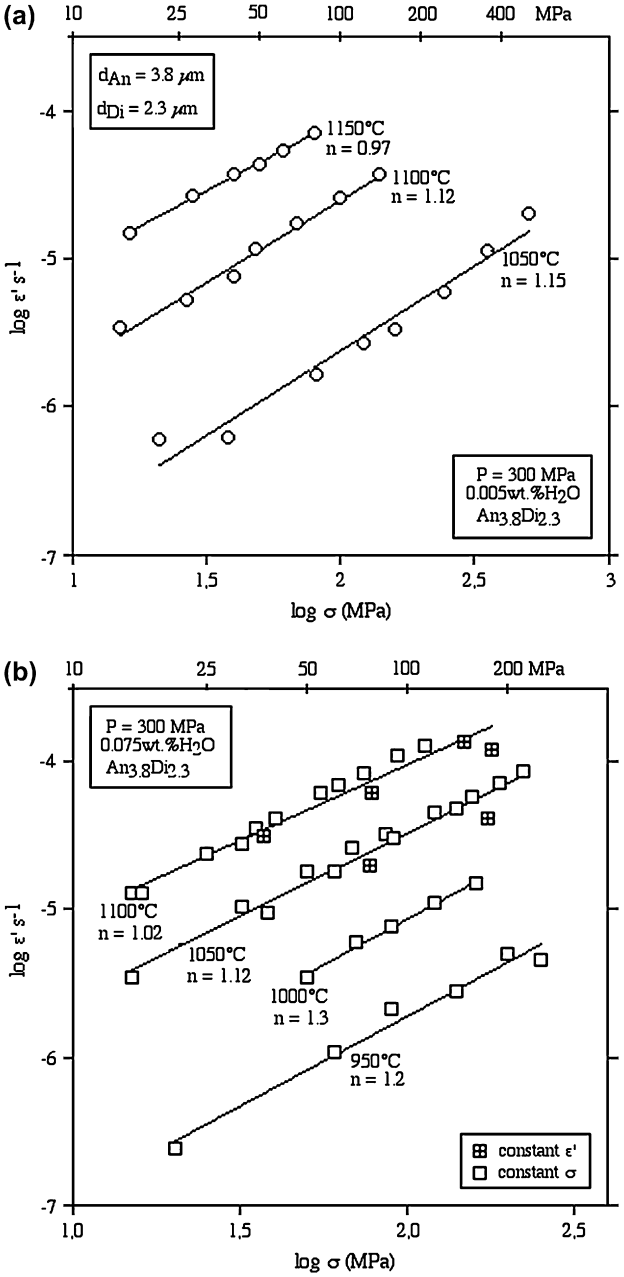

Fig. 6. Mechanical data for two-phase anorthite–diopside aggregates presented in log strain rate–log flow stress diagrams for different temperatures. Grain size of each phase (at the end of the experiment) is indicated by the subscript to each phase. (a) Dry samples deformed at 300 MPa in creep are characterized by a stress exponent n of ~1, indicating Newtonian flow. (b) Wet samples deformed at 300 MPa at constant stress (open squares) or at constant strain rates (crossed squares) are also characterized by stress exponents of $n \sim 1$.

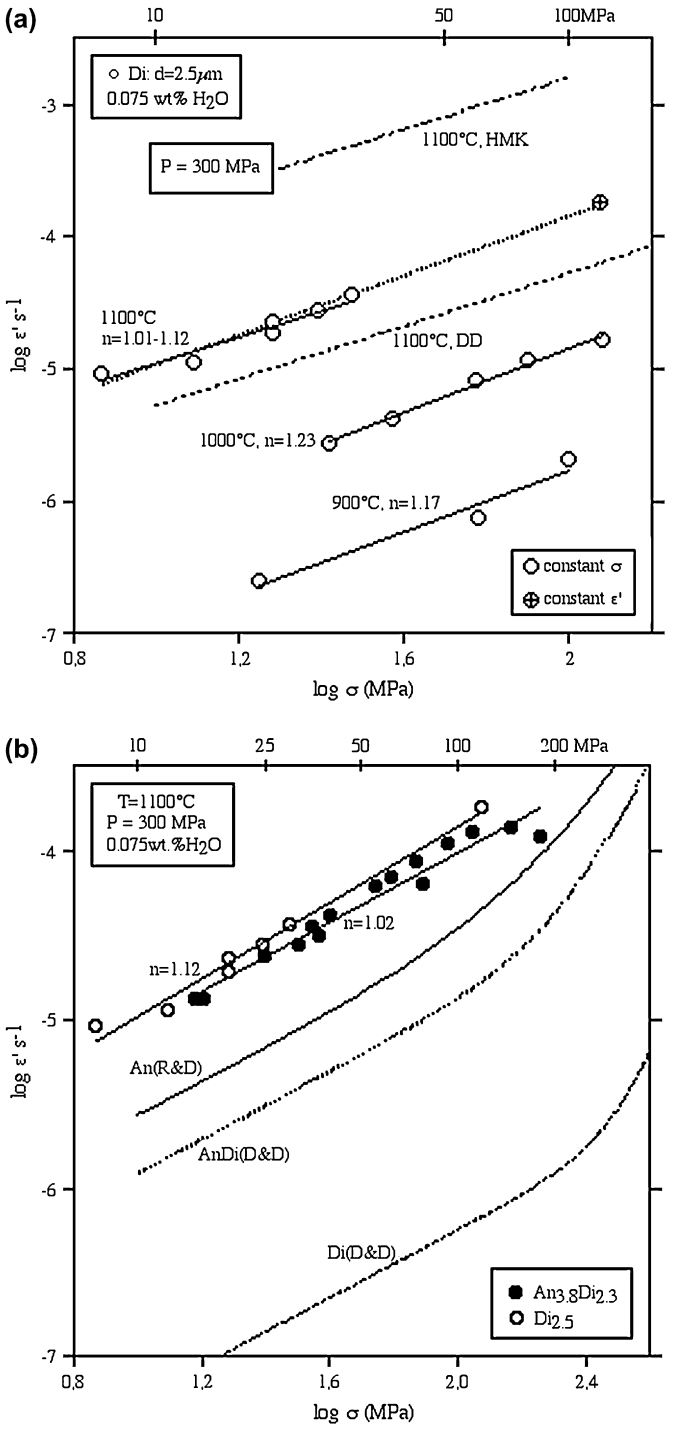

Fig. 7. Mechanical data for wet single-phase diopside (a) and two-phase anorthite–diopside aggregate (b) presented in log strain rate–log flow stress diagrams for different temperatures. (a) Open circles and crossed circle correspond to the present data obtained in constant stress and constant strain rate tests, respectively. We also show previous data for samples fabricated from natural diopside and recalculated to a grain size of 2.5 μm (DD: Dimanov and Dresen, 2005; HMK: Hier-Majumder et al., 2005). All samples show Newtonian flow. (b) Open and filled circles correspond to the present data for diopside and anorthite–diopside mixtures, respectively. We also show previous original data for anorthite (An(R&D): Rybacki and Dresen, 2000), for diopside (Di(D&D): Dimanov and Dresen, 2005), and for coarse diopside dispersion (50 vol%) in fine-grained anorthite matrix (AnDi(D&D): Dimanov and Dresen, 2005). Newtonian flow dominates at stresses <150–200 MPa.

factors may reflect differences found for the different materials, like crystal chemistry, point defect concentrations, and sample microstructure (i.e. grain size distribution). However, the similar activation energy likely indicates that grain boundary diffusion-controlled creep is dominant in all wet samples.

As for the single phases (Dimanov et al., 1999; Rybacki and Dresen, 2000; Dimanov and Dresen, 2005; Hier-Majumder et al., 2005) trace amounts of water significantly affect strain rates and activation energies of two-phase samples (Fig. 10b, Table 3). Wet anorthite–diopside aggregates were significantly weaker than nominally dry samples. At a confining pressure of 300 MPa the activation energy of wet samples deformed in axial compression is $Q = 363 \pm 49$ kJ/mol, which is substantially lower than the activation energy of nominally dry samples ($Q = 571 \pm 53$ kJ/mol). A similar result was reported by Dimanov and Dresen (2005) for anorthite–diopside samples prepared from anorthite glass and crushed natural diopside single crystals. Samples studied by Dimanov and Dresen (2005) are considerably stronger than the present samples, likely because of the coarse grain size of the dispersed diopside particles.

We also estimated the activation energy for diffusion-controlled creep of wet anorthite–diopside aggregates from torsion tests (Fig. 11). The temperature range of creep tests performed in torsion at 400 MPa pressure covered 110°C. Estimates of activation energy based solely on the temperature steps performed in constant twist rate tests (Fig. 11a) are similar to the average of the whole data set of temperatures performed on the three specimens ($Q = 319 \pm 64$ kJ/mol, Table 4) Strain does not significantly affect the activation energy or the pre-exponential factor, with similar values obtained for different shear strains from $\gamma \sim 1$ to $\gamma \sim 4$. The activation energies for diffusion-controlled creep of anorthite–diopside aggregates estimated from axial compression tests and from torsion tests are in good agreement. After correcting for the difference in water fugacity, the flow laws obtained from both types of experiments are quite similar (Fig. 11b).

3.2. Microstructures

Specimens deformed in axial compression to total strains up to ~28% showed only moderate flattening of the anorthite and diopside clusters. Irrespective of water content, dislocation densities remain low ($\rho \leq 10^{11}$ m^{-2}) for samples deformed in creep tests, at flow stresses from ~8 MPa to ~500 MPa. However, the sample ADSW00-b deformed at a constant strain rate of 1.2×10^{-4} s^{-1} showed moderate but continuous strain hardening up to a flow stress of ~120 MPa. For this sample, cell structures and subgrains were commonly observed in TEM and the dislocation density was higher, but varied between grains from $\rho \sim 10^{11}$ m^{-2} to 10^{13} m^{-2}.

Specimens deformed in torsion to total shear strains up to $\gamma \sim 5$ show a pronounced microstructural evolution. Remaining anorthite and diopside clusters were extremely flattened and elongated sub-parallel to the minimum compressive stress direction at about 40° to the shear plane (Fig. 12a and b,

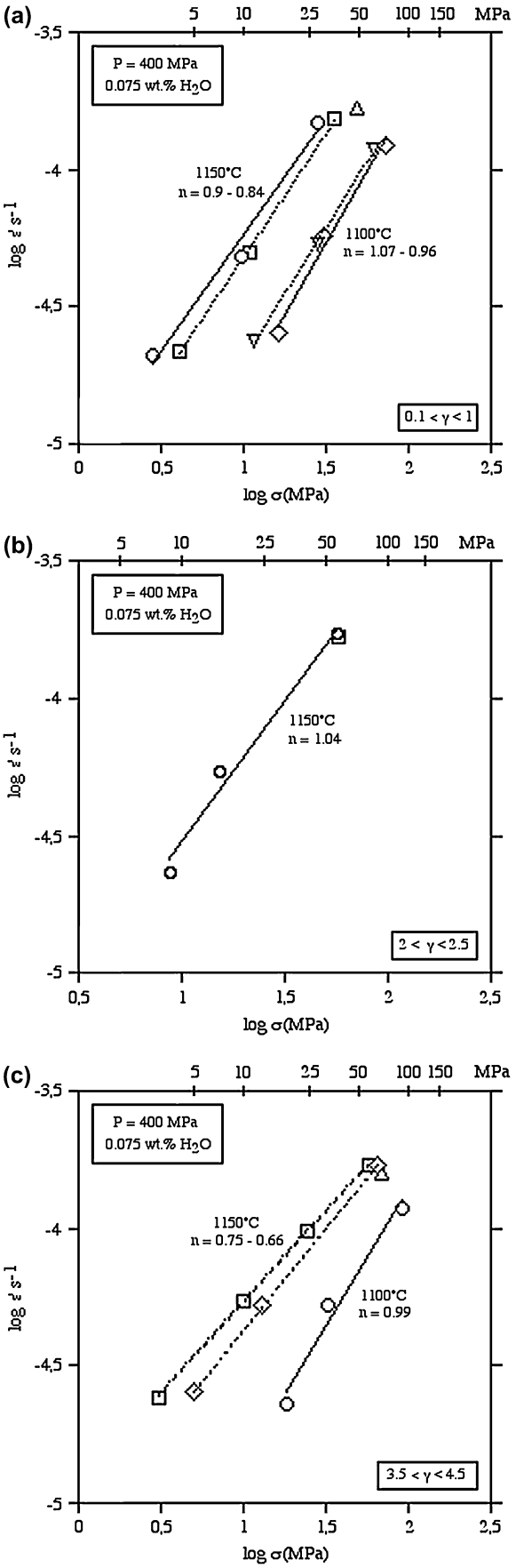

Fig. 8. Mechanical data for wet two-phase samples twisted at 400 MPa in constant twist rate stepping tests. The different symbols represent the results of individual twist rate stepping tests (see Fig. 5). The raw torsion data are first recalculated to shear stress and shear strain rate. To be compared with data from axial deformation they are recalculated to equivalent flow stress and strain rate (see text) and presented in log strain rate–log flow stress diagrams for different temperatures and strains: (a) low strain ($\gamma \sim 0.1-1$), squares and circles: ADSWT1, diamonds and inverted triangles: ADSWT2, triangle: ADSWT3; (b) intermediate strain ($\gamma \sim 2-2.5$) circles: ADSWT1, square: ADSWT3; (c) high strain ($\gamma \sim 3.5-4.5$), diamonds: ADSWT1, circles: ADSWT2, squares and triangles: ADSWT3. At the experimental flow stresses <100 MPa the stress exponents are $n \sim 1$, irrespective of strain.

ADSWT2). Abundant small pores are observed within the clusters with the highest aspect ratios (>5) and within the areas where complete phase mixing between diopside and anorthite grains occurred (Fig. 12b and c, ADSWT3). This mixing and the development of porosity is even more apparent in SEM micrographs from sections cut perpendicular to the sample axis (Fig. 13, sample ADSWT1). The almost undeformed specimen centre (Fig. 13a and b) shows separate and undeformed anorthite and diopside clusters. However, at the outermost rim of the specimen, where maximum strain accrued ($\gamma \sim 4.8$), grain-scale phase mixing occurred (Fig. 13c and d). In TEM, phase mixing was demonstrated using EDX (energy dispersive X-ray) mapping of Mg and Al, which allowed discrimination of individual diopside and anorthite grains. We did not observe substantial grain growth or refinement of diopside or anorthite grains during either axial or torsion deformation. However, we note that for twisted samples the largest anorthite grains are substantially less numerous within the areas of complete phase mixing (Fig. 12c) than they are in the original clusters (Fig. 13a) and remaining elongated clusters (Fig. 12b). Therefore, grain size refinement at high strains of the torsion experiments cannot be ruled out.

A striking observation from the outermost rims of all samples deformed in torsion (ADSWT1, ADSWT3, ADSWT3) was the formation of abundant voids and cavities along grain and phase boundaries. In areas of incomplete phase mixing, isolated pores at multiple grain junctions are very common in diopside clusters and at interphase boundaries, but are less common in anorthite clusters (Fig. 12b). Conversely, in areas of advanced phase mixing, porosity is more homogeneously distributed (Figs. 12c and 13d). Often, individual pores line up (cavitation coalescence) to form "strings" (Figs. 12b, 14a, b) that may interlink to form elongate open micocracks and fissures (Fig. 14b–f). These fissures are inclined by about 20°–25° to the shear plane and to the direction of maximum compressive stress. The longer fissures display a sigmoidal shape with shear offset. At a shear strain of $\gamma \sim 4.3$, the specimen ADSWT2 failed catastrophically during temperature stepping (Fig. 5b) forming an oblique fracture across the entire sample and extending within the alumina spacers with no visible shear offset.

In TEM, the presence of pores of several tens of nanometers in size is also commonly observed at diopside grain junctions and at anorthite–diopside phase boundaries (Fig. 15a and b). The pores are distinctly less rounded than fluid

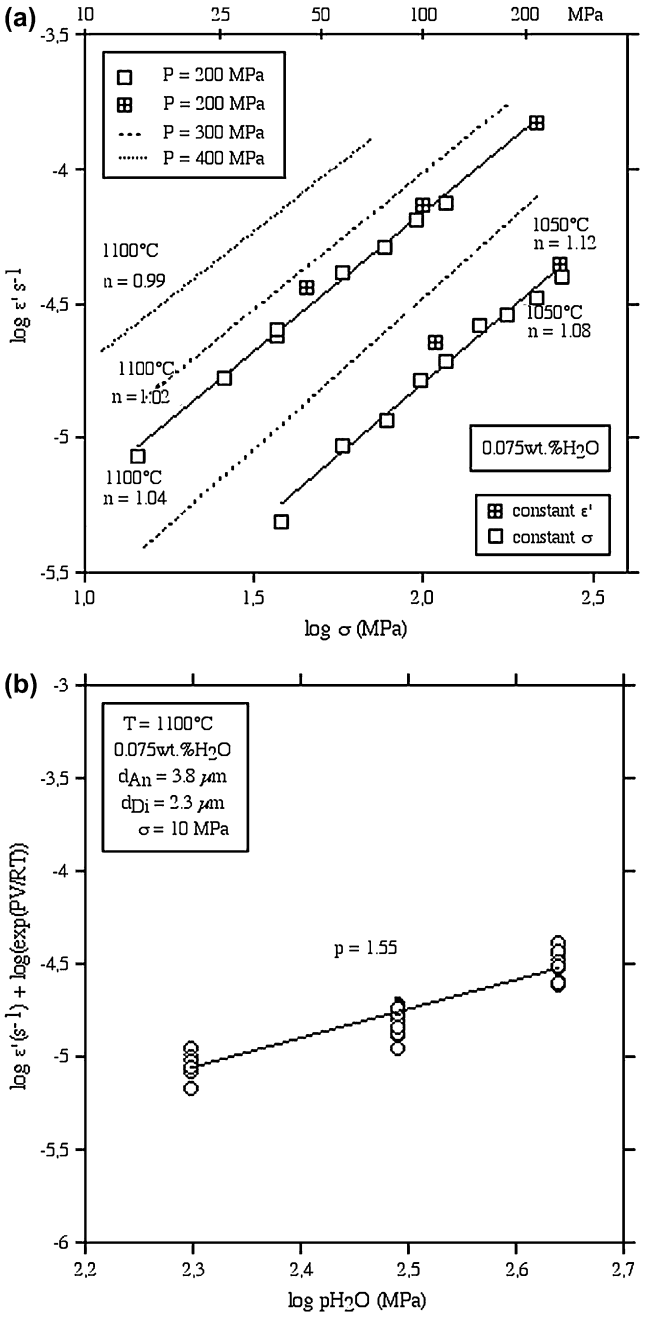

Fig. 9. Mechanical data for two-phase anorthite–diopside aggregates presented in log strain rate–log flow stress diagrams for different temperatures and confining pressures. (a) Wet samples deformed at 200 MPa confining pressure in creep (open squares) and constant strain rate (crossed squares). Stress exponent is $n \sim 1$. Data for axial and torsion tests at 300 MPa and 400 MPa confining pressure, respectively, are redrawn for comparison. (b) The mechanical data for wet two-phase samples deforming in linear-viscous creep presented in (b) are first recalculated to 10 MPa flow stress and recalculated for constant pressure using an activation volume estimated from literature (see text). Secondly the data are plotted versus water fugacity, yielding a water fugacity exponent $p = 1.55 \pm 0.25$, which is in close agreement with values for anorthite ($p = 1$, Rybacki et al., 2006) and diopside ($p = 1.4$, Hier-Majumder et al., 2005).

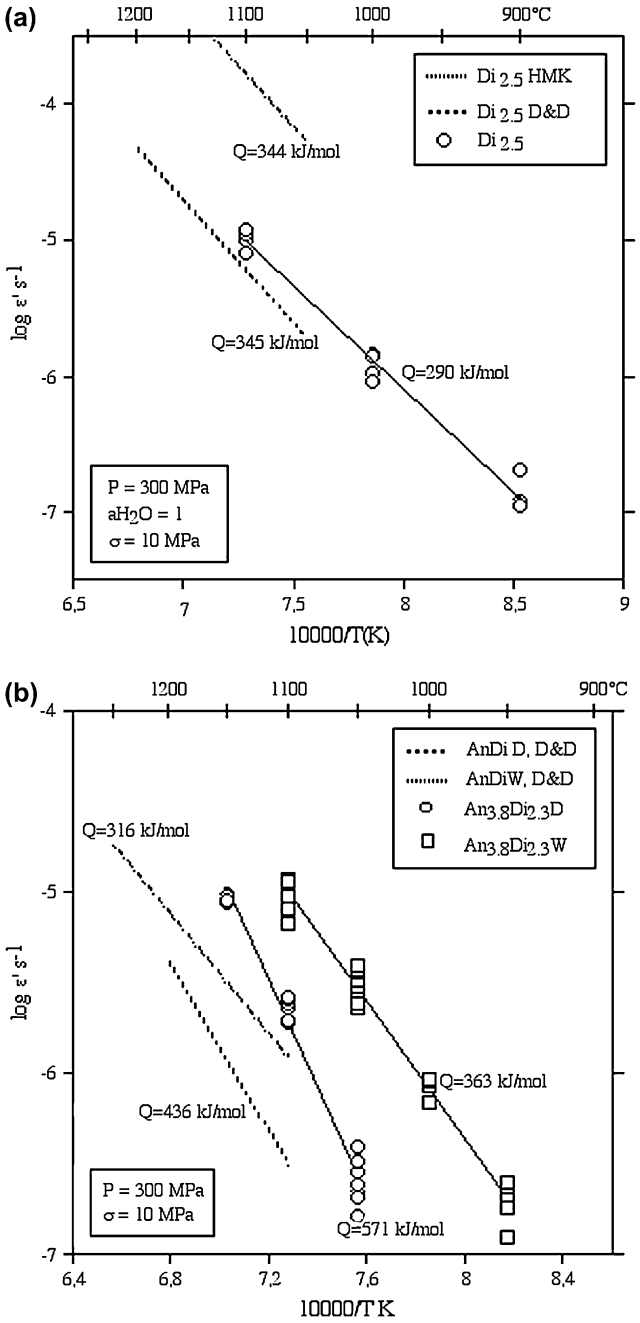

Fig. 10. Arrhenius diagrams for wet diopside (a) and for wet and dry anorthite–diopside mixtures (b). (a) Flow laws for wet diopside from three independent studies are in relatively good agreement, but iron-rich diopside (HMK) is weaker. (b) Linear-viscous creep of dry anorthite–diopside aggregates is characterized by substantially higher activation energy and lower strain rates than for wet samples. The same observation holds for data from Dimanov and Dresen (2005) for two-phase samples containing coarse grained diopside particles.

inclusions. Dislocation densities of deformed samples are between 10^{12} m^{-2} and 10^{13} m^{-2} (i.e. one to two orders of magnitude higher than in the starting material). The dislocation densities also exceed those resulting from coaxial creep testing (except for sample ADSW00-b). Dislocations are often curved and form networks and subgrain boundaries (Fig. 15b–d) suggesting that dislocation climb was active (Fig. 15). Grain boundary dislocations are frequent (Fig. 15b and c). Cell structures (Fig. 15d) may indicate recrystallization by subgrain rotation. Cavitation, cavitation coalescence, microfracturing and elevated dislocation densities only occur in samples deformed

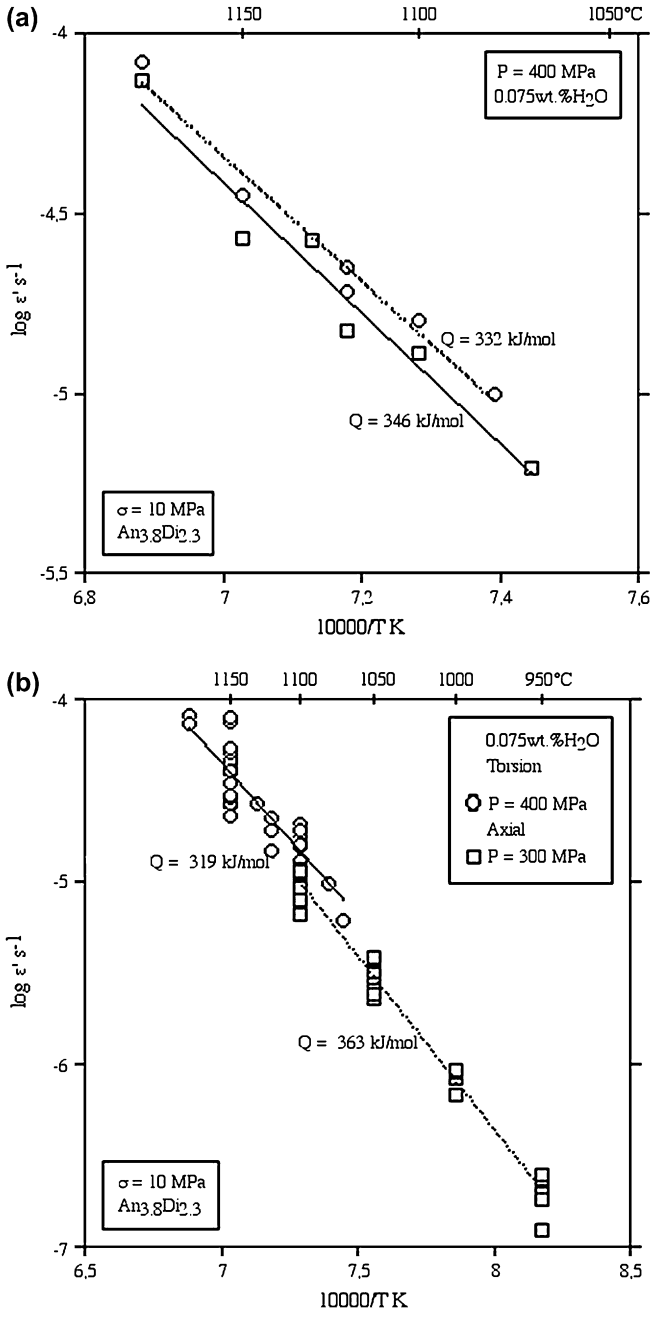

Fig. 11. Arrhenius diagrams for wet anorthite–diopside mixture deformed in torsion. (a) Data at moderate strain (open circles, $\gamma \sim 1$–1.5) and high strain (open squares, $\gamma \sim 4$). (b) Since data obtained at different strains are similar, we include all data from torsion tests irrespective of strain (open circles). The resulting estimate of the activation energy is in good agreement with estimates obtained from axial tests (open squares).

in torsion to high strains, indicating an evolving microstructure despite nearly constant stress and strain rate.

4. Discussion

4.1. Deformation mechanisms

The mechanical data from axial compression and torsion tests on hydrous and dry samples suggest a stress exponent of about $n = 1$ indicating linear-viscous (or Newtonian) creep. In previous experiments performed at similar stresses and temperatures on similar anorthite (Dimanov et al., 1999) and diopside (Dimanov et al., 2003; Hier-Majumder et al., 2005) aggregates, a grain size sensitivity of about $m = 3$ was reported. This value suggests that the creep rate is grain boundary diffusion rate limited (Coble, 1963) as opposed to dislocation accommodated mechanisms, which are assumed grain size insensitive. Dislocation densities remained constant at about $\rho \leq 10^{11}$ m^{-2}, similar to those observed in undeformed specimens, which also supports grain boundary diffusion as the main mass transfer mechanism for creep. However, purely diffusion-controlled creep must be accompanied by microstructural changes in grain shape corresponding to the macroscopic strain (flattening). In the present study individual feldspar and diopside grains remain approximately equant even at high shear strain (i.e. the grain shapes do not reflect the macroscopic strain). This observation indicates that on the grain scale, strain is largely accommodated by grain boundary sliding as is typically found in fine-grained superplastic materials. In general, superplastic fine-grained metals, ceramics (Nieh et al., 1997) and rocks (Paterson, 1990) are materials capable of sustaining very high strains under uniaxial tension before rupture. Usually such materials fail at high strain due to cavitation and cavitation coalescence (Onck and van der Giessen, 1998; Tekeli, 2002; Bae and Ghosh, 2000), which is also what we observed in our samples deformed in torsion at shear strains of $\gamma \approx 4.5$. In general, the physical mechanisms accommodating large-strain deformation of fine-grained engineering materials and rocks are not very well understood (Langdon, 1995; Nieh et al., 1997; Paterson, 1990; Wakai et al., 1999). In particular, it is difficult to discriminate between different potentially rate-limiting micromechanisms based on existing mechanical data and microstructure (Zelin and Mukherjee, 1996). Experimental observations on different materials have spawned a variety of phenomenological models that typically assume grain boundary sliding accommodated by dislocation activity and/or grain boundary diffusion as end-member cases (Nieh et al., 1997). The proposed models predict stress exponents of $n = 1$ and $n = 2$ for grain boundary sliding rate limited by diffusion and dislocation activity, respectively. Depending on the model, a grain size sensitivity of $m = 2$ or $m = 3$ is assumed. In this study, the cavitation phenomenon and the stress exponents estimated from axial compression and torsion experiments on diopside and anorthite–diopside aggregates ($n \approx 1$) are in agreement with diffusion-controlled grain boundary sliding. However, grain boundary dislocation microstructures and possible indications of recrystallization suggest partial accommodation of grain boundary sliding by dislocation activity.

In general, microstructures in specimens deformed in axial compression did not differ significantly from those observed in the undeformed samples. The dislocation densities remained at about $\rho \leq 10^{11}$ m^{-2} and individual grains remained equant, although single-phase clusters were somewhat flattened. A single specimen ADSW00-b, developed dislocation densities that were significantly higher than in the starting material ($\rho \approx$

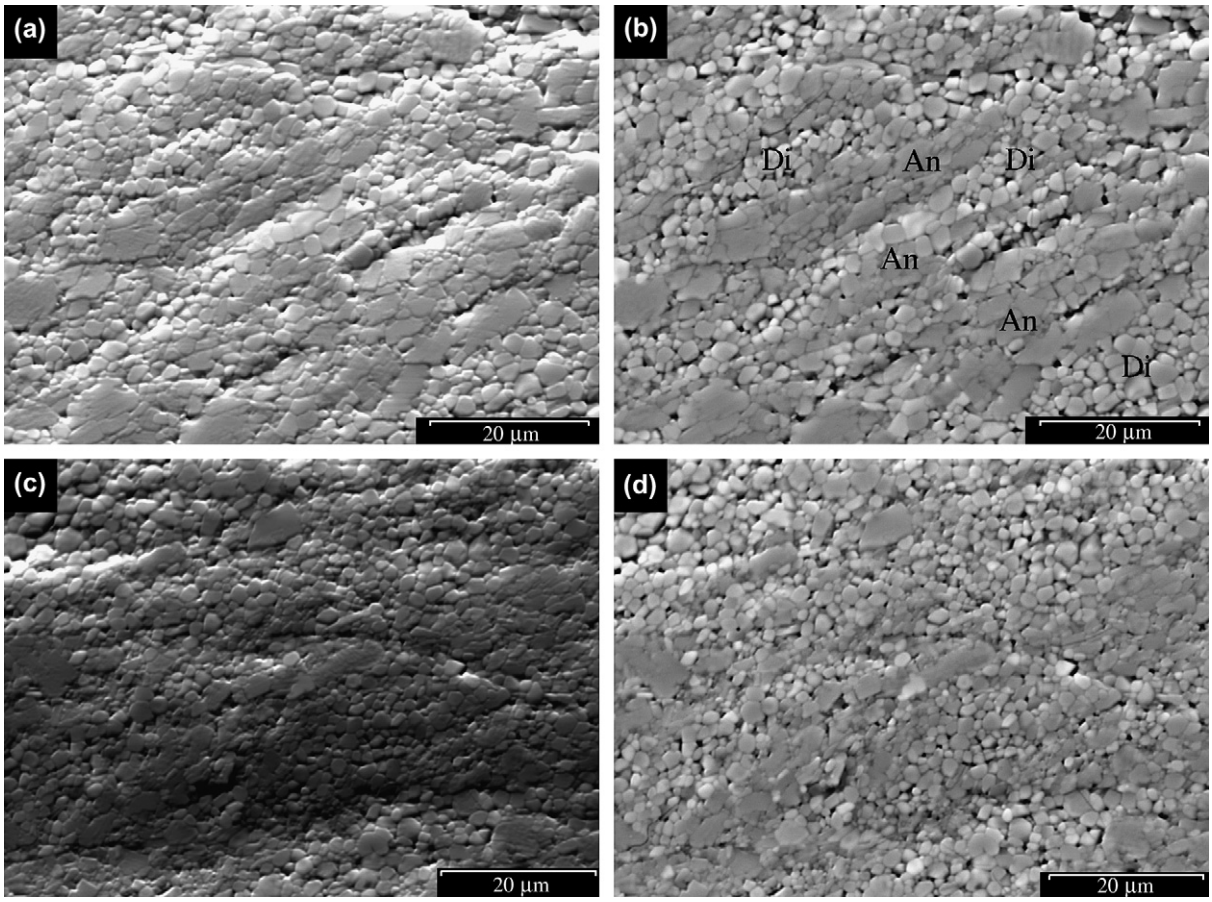

Fig. 12. SEM micrographs from a tangential section (parallel to the axis) of twisted specimen AnDiSW3 deformed at 1150°C to $\gamma \sim 4.8$. Shear sense is dextral. (a) Close to the sample rim remaining phase clusters are extremely elongated. (b) Same as (a) in BSE (back scattered electrons) mode. Anorthite and diopside appear in dark and light grey, respectively. Anorthite is somewhat finer grained than in the starting clusters. Porosity from cavitation appears in black and is more pronounced in diopside clusters and at interphases. (c) Most of the sample rim exhibits grain-scale mixing. (d) Same as (c) in BSE mode. Pores/cavities are more homogeneously distributed when phase mixing occurs than in preserved clusters.

10^{12} m^{-2}); this sample was shortened 26% at a uniform strain rate of 1.2×10^{-4} s^{-1} and did show moderate strain hardening (from 130 MPa to 170 MPa flow stress).

The microstructures of samples deformed in torsion at similar strain rates show that the individual anorthite and diopside grains remain equant, but dislocation densities are higher ($\rho = 10^{12}$ m^{-2}–10^{13} m^{-2}) for both phases than in the undeformed specimens. The large single-phase clusters are extremely flattened. In addition, grain-scale phase mixing and cavitation are widespread. The dislocation microstructures suggest that, at low strain, grain sliding may have been largely accommodated by grain boundary diffusion-controlled creep. However, our observations indicate that enhanced dislocation slip and/or climb contributes significantly to strain accommodation in samples deformed to large total strain.

A striking observation of this study is that the constitutive flow laws remain very similar at different strains and strain rates, irrespective of the different microstructures found in specimens deformed to different total strains and at different strain rates. In particular, the stress exponent $n \approx 1$ for all experiments performed in this study, indicating linear-viscous deformation. Although we observe evidence for dislocation activity at high strain, theoretical models for grain boundary sliding accommodated by dislocation creep predict a stress exponent of $n = 2$ that is inconsistent with our measurement of $n \approx 1$. We are not aware of any mechanical model predicting linear-viscous flow, a grain size sensitivity $m > 2$ and a strain-dependent evolution of the dislocation microstructure at constant stress. The microstructural observations of highly strained samples suggest that dislocations are emitted at grain triple junctions (Fig. 15d) and in the grain boundary region (Fig. 15b and c). The mobility of the grain boundary dislocations is likely climb controlled, because the dislocations are mostly curved and cell structures and subgrains are common. Activation energies for samples deformed to low and high strains (higher dislocation density) are similar, and thus we assume that the mechanisms rate-limiting deformation, are also similar in both cases.

4.2. Grain boundary diffusion processes

Theoretically, grain boundaries may act as sources and sinks for vacancies. Local stress gradients induce chemical potential gradients inducing vacancy diffusion and molecular

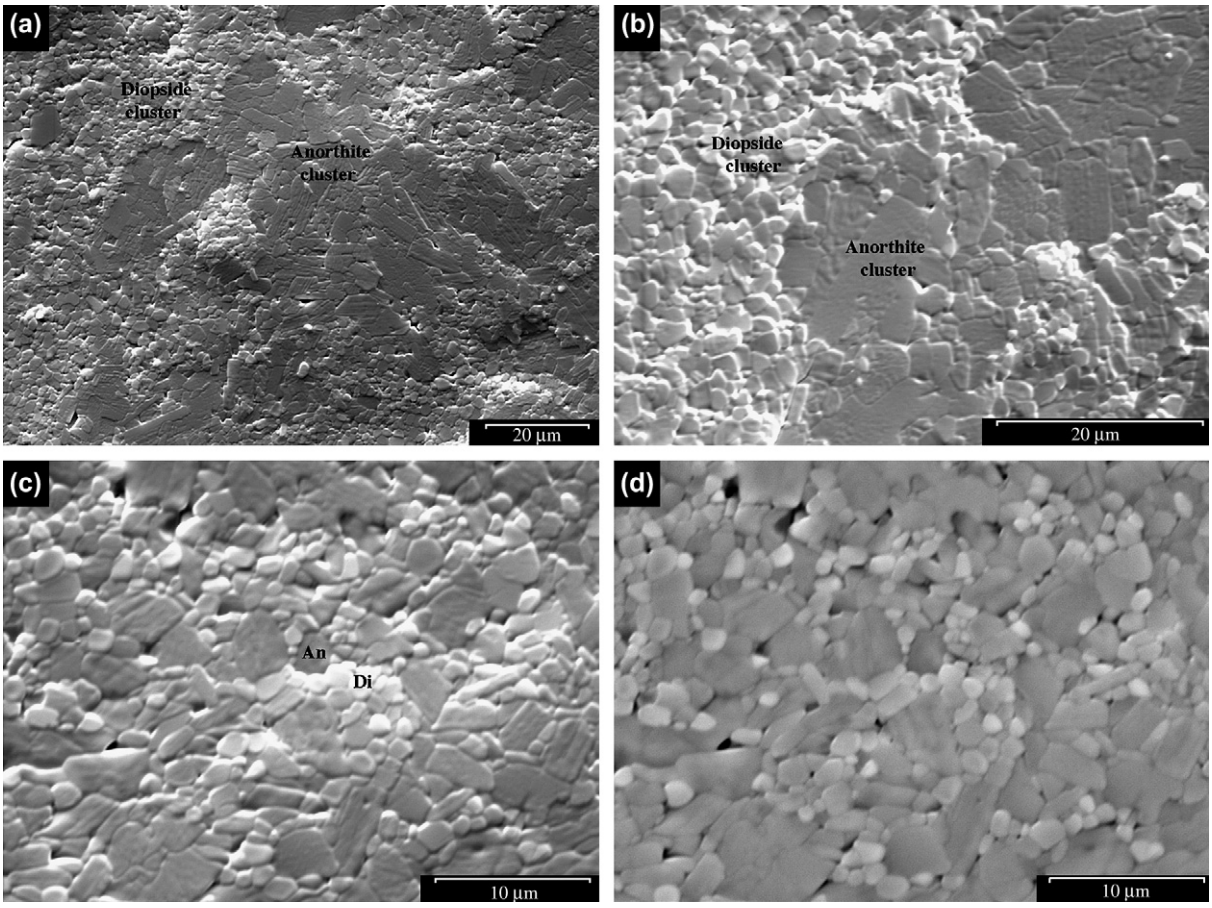

Fig. 13. SEM micrographs from a transverse section (perpendicular to the axis) of twisted specimen AnDiSW2 deformed at 1080–1120°C to $\gamma \sim 4.3$. (a and b) In the central part of the section, with virtually no strain, there is little change of the microstructure, and large single-phase clusters persist. (c) At the rim of the section, with a maximum shear strain ($\gamma \sim 4.3$), the microstructure changes dramatically with extensive grain-scale phase mixing. (d) Same as (c) in BSE (back scattering mode). Substantial cavitation is observed.

counter diffusion of material along grain boundaries which control the deformation rate in fine-grained materials (Coble, 1963). During superplastic deformation of Al–Mg alloy, high concentration of vacancies at grain boundaries has been evidenced by the presence of nanometer sized voids that form along grain boundaries upon cooling (Vetrano et al., 1999). Coble creep and diffusion-controlled grain boundary sliding are characterized by Newtonian flow ($n = 1$) and a strong grain size sensitivity ($m = 3$). Previous studies performed on synthetic anorthite and diopside end members (Wang et al., 1996; Dimanov et al., 1999; Rybacki and Dresen, 2000; Dimanov et al., 2003; Hier-Majumder et al., 2005) suggested grain boundary diffusion-controlled creep at thermodynamic conditions similar to the conditions explored in the present study. These studies were based on coaxial deformation with maximum strains between 10% and 30%. Our observations suggest that the deformation mechanisms operating in the samples deformed in axial compression in this study are similar.

For grain boundary diffusion-controlled creep, some polyphase mixtures were thought to be weaker than the pure end members (Bruhn et al., 1999; Farver and Yund, 1995; Wheeler, 1992). This behaviour has been partly attributed to chemical reactions between neighbouring phases and/or enhanced diffusivities of interphase boundaries compared to grain boundaries. For example, the difference in crystallographic structure between adjacent anorthite and diopside grains and limited mutual exchange of Al, Ca, and Mg will likely produce phase boundaries distinctly different from grain boundaries of the pure end-member phases. The axial deformation and torsion data yield very similar stress exponents and activation energies indicating that phase mixing and associated increase of phase boundaries have no effect on the constitutive parameters. This observation suggests that the varying abundance of grain and phase boundaries does not affect the rate-controlling creep mechanism operating in hydrous samples.

For anhydrous samples with a similar range in grain size, Dimanov et al. (2003) found that the flow strength of diopside is about one order of magnitude higher than of anorthite. Bystricky and Mackwell (2001) and Dimanov and Dresen (2005) report that water-bearing diopside is somewhat stronger than hydrous anorthite (Rybacki and Dresen, 2000). From simple continuum mechanics and mixing models, diopside-bearing two-phase specimens are expected to be less viscous than pure diopside aggregates (Yoon and Chen, 1990;

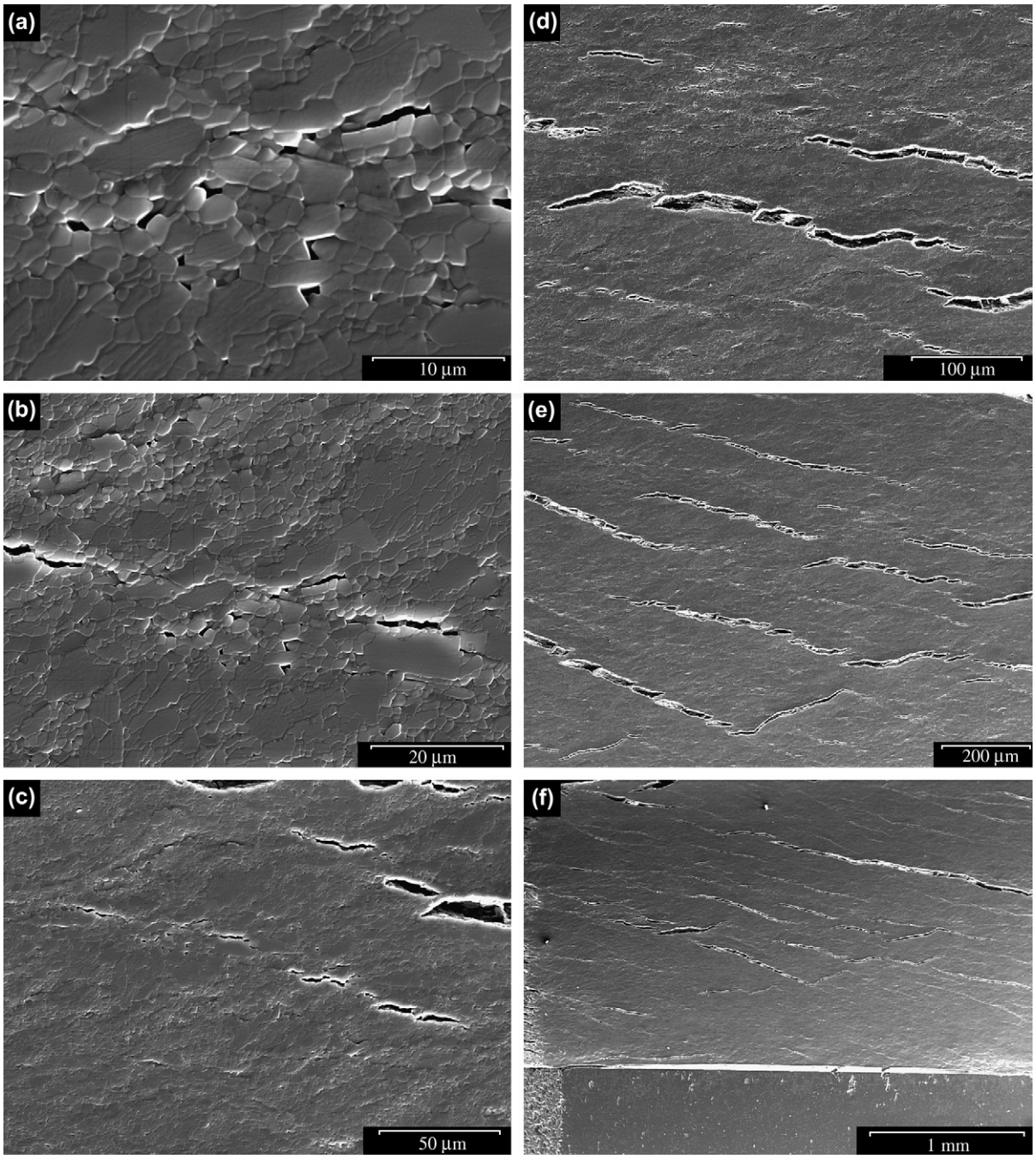

Fig. 14. SEM micrographs from a tangential section (parallel to the axis) of twisted specimen ADSWT3 deformed at 1150°C to $\gamma \sim 4.8$. Shear sense is horizontal dextral. (a) At high magnification, grain-scale cavitation is evident; individual pores lie at multiple grain junction, some pores are connected by micro-cracks at grain boundaries (coalescence). (b and c) Cavitation coalescence results in micro-fissures along tens of grains. The fissures line up at 20°–30° to the shear plane. (d and e) Linking of micro-fissures results in the formation of micro-cracks and s-shaped meso-cracks, hundreds of micrometers in length. (e) Linking of the s-shaped meso-cracks. (f) Overview of the sample (and the alumina spacer at the bottom) showing the extensive development of macro-cracks by cavitation and cavitation coalescence during ductile flow.

Tullis et al., 1991; Ravichandran and Seetharaman, 1993). In contrast, creep strength of pure diopside specimens and anorthite–diopside mixtures are quite similar (Fig. 7b). In the two-phase aggregates deformed in this study, the grain size of diopside is about 65% smaller than of anorthite, and thus the effective strength contrast between the two phases is significantly reduced.

4.3. Grain boundary sliding and cavitation

Samples deformed in torsion at constant shear strain rates and flow stresses of about 3×10^{-5}–3×10^{-4} s^{-1} and 30–65 MPa, respectively, show abundant cavities evolving with strain. Interlinkage of cavities is observed, eventually leading to catastrophic failure. Voids and cracks line up to form

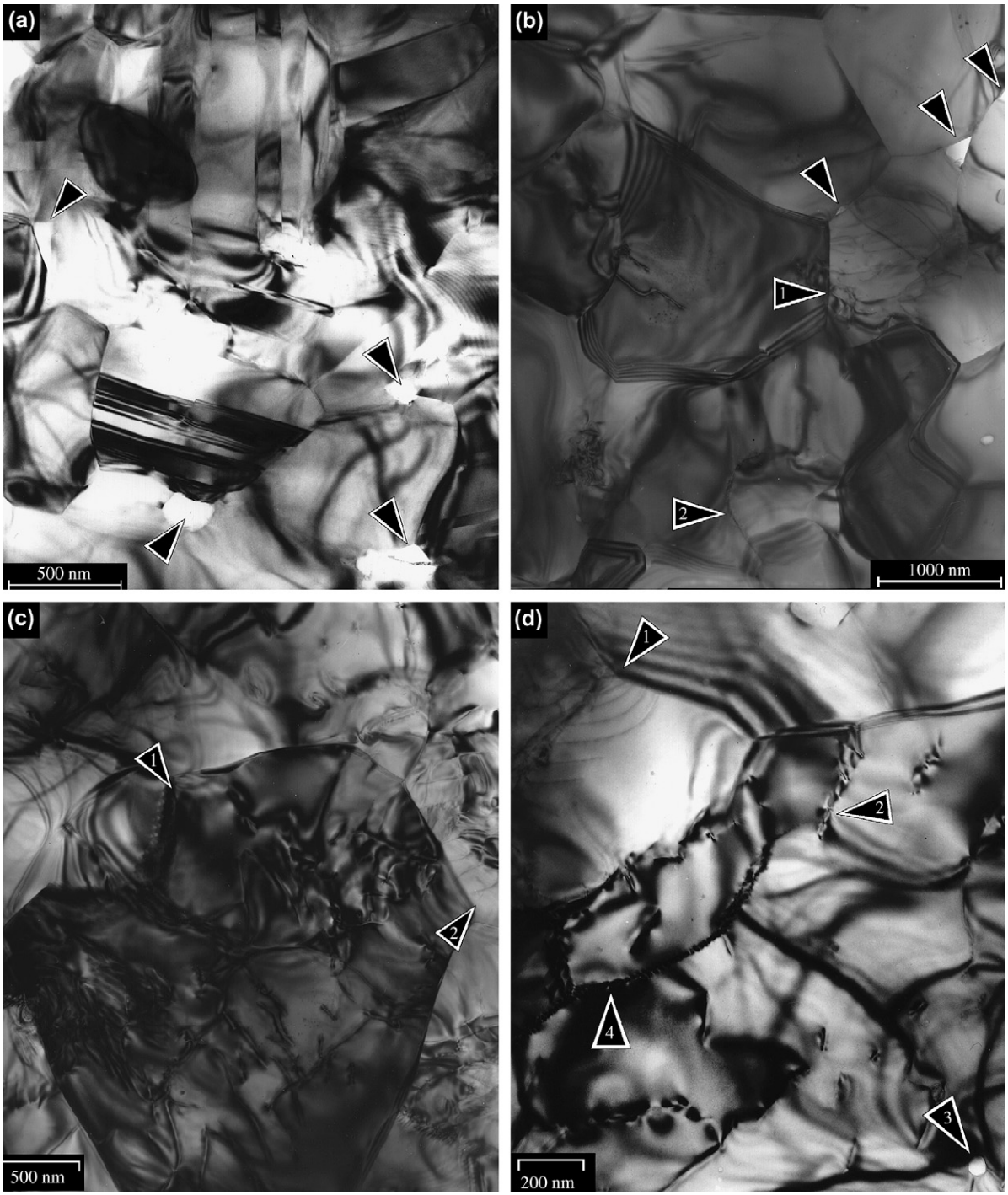

Fig. 15. TEM micrographs of twisted specimen ADSWT3 deformed at 1150°C to $\gamma \sim 4.8$. (a) Cavities are shown (arrows) at multiple grain junctions and phase boundaries. (b) Cavitation (arrows) and enhanced dislocation densities in remaining small diopside cluster. Arrow 1 points to grain boundary dislocations and arrow 2 points to a subgrain boundary. (c) Area with very high dislocation density. Arrow 1 points to a subgrain boundary in a heavily deformed diopside grain and arrow 2 points to an interface showing grain boundary dislocations. (d) Arrow 1 points to a triple junction emitting curved dislocations. Arrow 2 points to a dislocation wall. Arrow 3 points to a cavity forming at a triple junction. Arrow 4 points to evolved cell structures. Arrows 1, 2 and 4 point to features suggesting recrystallization by subgrain rotation.

fissures inclined about 20°–30° to the maximum compression direction. We did not specifically investigate how far these fissures extend toward the centre of the specimen, but they seem to be limited to the outer rim (at the largest strain). The fissures appear regularly spaced (Figs. 14 and 16). Cavitation is commonly observed in superplastic flow of metals, alloys and ceramics (Kassner and Hayes, 2003; Nieh et al., 1997), however, in room pressure experiments. Elevated confining pressures have been found to reduce cavitation in ceramics (Bampton et al., 1983; Pilling and Ridley, 1988). Paterson

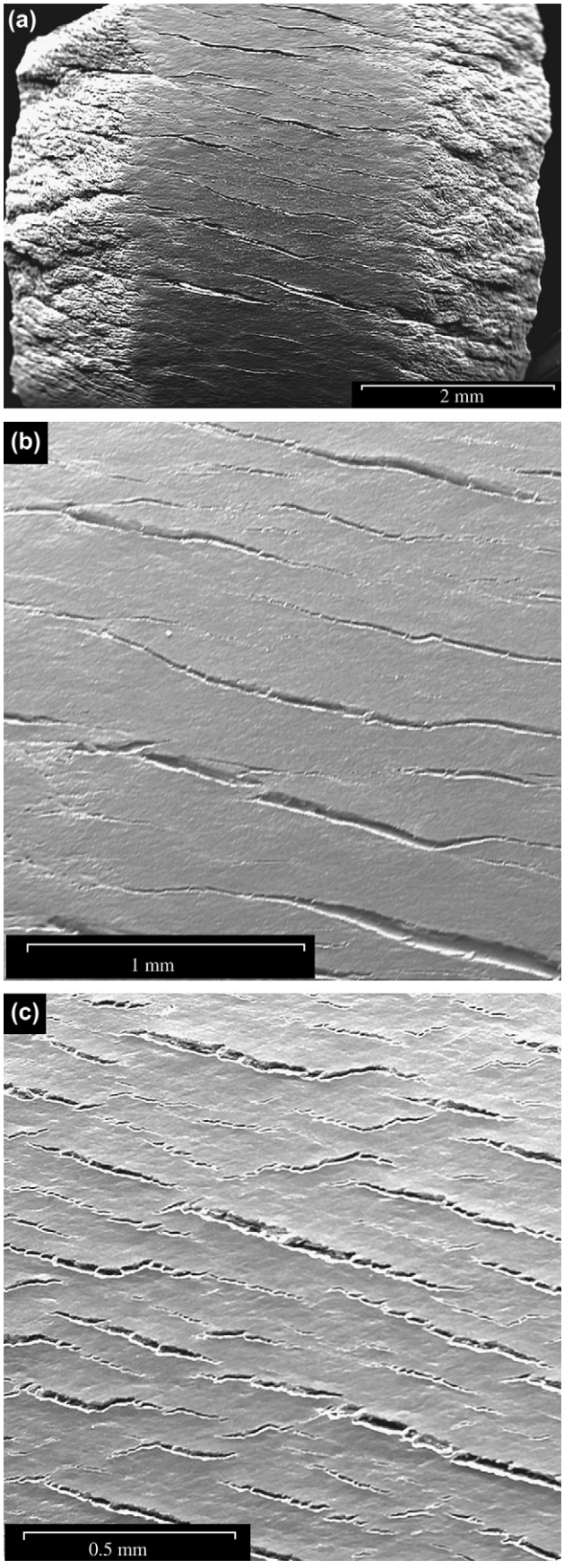

(1990) suggested that under geological conditions voids are unlikely to form in rocks when flow stress is comparable to the lithostatic pressure. Yet, from some field studies on fine-grained mylonite rocks deformed at elevated pressures, there is some evidence for cavitation (White and White, 1983; Behrmann, 1985; Behrmann and Mainprice, 1987). Our torsion experiments clearly demonstrate that cavities form in geological materials at flow stresses significantly less than the effective confining pressure.

Depending on temperature, confining pressure and stress conditions, cavities may nucleate by grain boundary debonding at points of high local stress concentration, such as dislocation pile-ups (Zener, 1948) or by coalescence of vacancies (Vetrano et al., 1999). Typical nucleation sites are grain boundary ledges and steps, grain triple junctions, intersections of twin and grain boundaries, and phase boundaries. Once nucleated, voids and cavities may grow by continued vacancy condensation, by plastic deformation of material surrounding the cavity, or by propagation of brittle cracks due to stress concentration around the cavities (Chokshi and Langdon, 1991; Riedel, 1993). During deformation, local stresses will also increase with strain and time by work hardening associated with dislocation pile-up and grain growth. Formation of cavities will likely contribute to an increase of local stresses promoting dislocation activity and cracking. In the feldspar–diopside aggregates, abundant cavities were only observed in samples deformed to large strain in torsion but not in low-strain axial compression, even for sample ADSW00-b deformed at high stresses and exhibiting high dislocation densities. Strain-dependent cavity growth is also reported for ceramic composites (Nieh et al., 1997).

When stresses are not relaxed sufficiently fast by diffusion and/or intracrystalline plasticity they will quickly exceed grain boundary cohesion (Chen and Xue, 1990; Evans et al., 1980; Kim et al., 2001; Nieh et al., 1997). The cohesive strength of grain boundaries depends on the ratio of surface energy to grain boundary energy; both are a function of chemical composition and impurity content in the boundary region. In ceramics liquid films wetting the crystal boundaries were thought to reduce local stresses, but the effect on cavity nucleation rate is not clear (Evans et al., 1980; Nieh et al., 1997). Diffusive stress relaxation and vacancy coalescence depend on interface reactions, diffusivities of grain and phase boundaries and transport width, a parameter that likely correlates with grain size and grain shape. In our samples, cavities appear to form more readily at interphase boundaries and in fine-grained diopside clusters (Figs. 12 and 14), which may indicate faster grain boundary sliding-rates for the equant diopside grains.

Fig. 16. SEM micrographs of twisted specimens ADSWT3 (a and b) and ADSWT2 (c). Shear sense is horizontal dextral. (a and b) Overviews of macro-cracks formed by cavitation and coalescence during ductile flow at 1150°C. (c) Overviews of macro-cracks formed by cavitation and coalescence during ductile flow at 1100°C. For a comparable finite strain the damage density is substantially higher at lower temperature. Note the different scale.

5. Conclusions and geological implications

The strength of the upper lithosphere may be largely controlled by the behaviour of high-temperature shear zones (Burlini and Bruhn, 2005; Kenner and Segall, 2003). Fine-grained ultramylonites in the Earth's lower continental crust are often composed of homogeneous mixtures of mainly feldspar, pyroxene and amphibole. It has been frequently suggested that highly strained ultramylonites deform by diffusion-accommodated grain boundary sliding (Behrmann and Mainprice, 1987; Steffen et al., 2001; Kenkmann and Dresen, 2002). Typical microstructures that are considered to indicate grain boundary sliding are equant grains, a low dislocation density and the presence of voids along straight grain boundaries (Passchier and Trouw, 1996). However, often ultramylonites also show enhanced dislocation densities, recrystallized grains and lattice preferred orientations indicating at least a component of dislocation creep (Behrmann and Mainprice, 1987; Kenkmann and Dresen, 2002). Therefore, inferring the dominant deformation mechanism from microstructures observed in natural ultramylonites remains non-unique. Identification of the prevailing mechanical flow law is a prerequisite for estimating lithospheric strength and its variation with temperature, pressure, stress and grain size.

Our experiments on fine-grained synthetic diopside–anorthite aggregates clearly show an evolution of microstructure with increasing strain up to $\gamma \sim 4.5$. The microstructure evolution includes (a) an increasing contribution of dislocation activity, (b) mechanical mixing of mineral phases, and (c) a marked increase of porosity by cavitation. The grain shape in deformed specimens remains almost equant, independent of strain. Remarkably, the mechanical data do not reflect the development of the microstructural changes. The strength, stress exponent, and activation energy that define the constitutive behaviour of the material remain almost constant irrespective of strain suggesting steady-state deformation. Clearly, the ''microstructural state'' is not obviously representative of the ''mechanical state''. This observation raises the question of identifying adequate state variables for constitutive equations of high-temperature creep of polyphase rocks (Evans, 2005).

Commonly, microstructures of exposed mylonites are compared to their experimentally produced counterparts assuming a steady state. This comparison is then often used to infer the prevailing deformation mechanism operating in the field. However, our experiments show that local observations of the microstructure are not unique identifiers of the bulk mechanical behaviour. For example, the increasing dislocation density with increasing strain observed at a constant stress strongly suggests that dislocation density paleopiezometers provide only a local estimate of the stress, which may differ from the average, remotely applied stress. Kenkmann and Dresen (1998, 2002) inferred competing grain boundary sliding accommodated by diffusion and dislocation creep to operate on a local (grain) scale within natural ultramylonites. Similar competitions between intracrystalline and intercrystalline deformation mechanisms were also suggested for eclogites (Godard and van Roermund, 1995; Mauler et al., 2001). However, this observation may not necessarily indicate that deformation occurs at the transition between two deformation regimes. Instead, our results strongly suggest that linear-viscous flow accommodated by grain boundary sliding may largely dominate the bulk rheology of ultramylonites.

In shear zones a transition may occur with increasing strain from mylonites with a pronounced compositional layering and strong lattice preferred orientation to ultramylonites with homogeneously mixed phases and weak to no lattice preferred orientation. Phase mixing may result from preferential nucleation of unlike-phases and neocrystallization, driven by the minimisation of interfacial energy (Kruse and Stünitz, 1999) or stress-induced gradients of the chemical potential (Kenkmann and Dresen, 2002). Our results show that mechanical mixing by grain boundary sliding is itself an important mechanism to homogenize phase distributions in ultramylonites at high temperatures. Abundant interphase boundaries will suppress further grain growth and stabilize the grain size, and hence promote linear-viscous creep.

The strong increase of pore volume with strain at high confinement, generated by nucleation, growth, and interconnection of cavities during grain sliding may affect the permeability of fine-grained mylonites, resulting in enhanced fluid flow. In accord with previous studies on single-phase samples, our experiments with anorthite–diopside aggregates show that high-temperature deformation rates, and for instance grain sliding kinetics, strongly increase with water fugacity. Thus, enhanced aqueous fluid flow and water fugacity could possibly trigger further porosity development in the ultramylonite. The catastrophic failure of the wet, high-strain samples related to cavitation at high pressure and high temperature indicates that dynamic instabilities may nucleate at lower-crustal depth.

Acknowledgements

We warmly thank Jan Tullis and an anonymous reviewer for their concise and constructive reviews which significantly improved the manuscript. We also thank M. Naumann for his help with the torsion tests, and S. Gehrmann and K. Paech for thin section preparation.

References

Allison, I., Barnett, R.L., Kerrich, R., 1979. Superplastic flow and changes in crystal chemistry of feldspars. Tectonophysics 53, T41–T46.

Bae, D.H., Ghosh, A.K., 2000. Grain size and temperature dependence of superplastic deformation in an Al-Mg alloy under isostructural condition. Acta Mater. 48, 1207–1224.

Bampton, C.C., Mahoney, M.W., Hamilton, C.H., Ghosh, A.K., Raj, R., 1983. Control of superplastic cavitation by hydrostatic pressure. Metall. Trans. 14A, 1583–1591.

Behrmann, J.H., 1985. Crystal plasticity and superplasticity in quartzite; a natural example. Tectonophysics 115 (1–2), 101–129.

Behrmann, J.H., Mainprice, D., 1987. Deformation mechanisms in a high-temperature quartz-feldspar mylonite: evidence for superplastic flow in the lower continental crust. Tectonophysics 140, 297–305.

Bell, D.R., Ihinger, P.D., Rossman, G.R., 1995. Quantitative analysis of trace OH in garnet and pyroxenes. Am. Mineral. 80, 465–474.

Beran, A., 1976. Messung des Ultrarot - Pleochroismus von Mineralen. XIV. Der Pleochroismus der OH-Streckfrequenz in Diopsid. Tschermaks Mineral Petrogr. Mitt. 23, 79–85.

Beran, A., 1986. A model of water allocation in alcali feldspar, derived from infrared-spectroscopic investigations. Phys. Chem. Miner. 13, 306–310.

Beran, A., 1987. OH groups in nominally anhydrous framework structures: An infrared spectroscopic investigation of danburite and labradorite. Phys. Chem. Miner. 14, 441–445.

Boullier, A.M., Gueguen, Y., 1975. SP-Mylonites: origin of some mylonites by superplastic flow. Contrib. Mineral. Petrol. 50, 93–104.

Bourne, S.J., 2003. Contrast of elastic properties between rock layers as a mechanism for the initiation and orientation of tensile failure under uniform remote compression. J. Geophys. Res. 108 (B8), 2395, doi:10.1029/2001JB001725.

Bromiley, G.D., Keppler, H., McCammon, C., Bromiley, F.A., Jacobsen, S.D., 2004. Hydrogen solubility and speciation in natural, gem-quality chromian diopside. Am. Mineral. 89, 941–949.

Bruhn, D.F., Olgaard, D.L., Dell'Angelo, L.N., 1999. Evidence for enhanced deformation in two-phase rocks: experiments on the rheology of calcite–anhydrite aggregates. J. Geophys. Res. 104 (B1), 707–724.

Bürgmann, R., Ergintav, S., Segall, P., Hearn, E.H., McClusky, S., Reilinger, R.E., Woith, H., Zschau, J., 2002. Time-dependent distributed afterslip on and deep below the Izmit earthquake rupture. Bull. Seismol. Soc. Am. 92 (1), 126–137.

Burlini, L., Bruhn, D., 2005. High-strain zones: laboratory perspectives on strain softening during ductile deformation. In: Bruhn, D., Burlini, L. (Eds.), High-Strain Zones: Structure and Physical Properties. Geological Society, London, Special Publications, vol. 245, pp. 1–24.

Bystricky, M., Mackwell, S., 2001. Creep of dry clinopyroxenite aggregates. J. Geophys. Res. 106 (B7), 13443–13454.

Chen, I.W., Xue, L.A., 1990. Development of superplastic structural ceramics. J. Am. Ceram. Soc. 73, 2585–2609.

Chokshi, A.H., Langdon, T.G., 1991. Overview: characteristics of creep deformation in ceramics. Mater. Sci. Technol. 7, 577–584.

Coble, R.L., 1963. A model for boundary diffusion controlled creep in polycrystalline materials. J. Appl. Phys. 34, 1679–1682.

Dimanov, A., Dresen, G., 2005. Rheology of synthetic anorthite–diopside aggregates: implications for ductile shear zones. J. Geophys. Res. 110, B07203, doi:10.1029/2004JB003431.

Dimanov, A., Dresen, G., Wirth, R., 1998. High-temperature creep of partially molten plagioclase aggregates. J. Geophys. Res. 103, 9651–9664.

Dimanov, A., Lavie, M.P., Dresen, G., Ingrin, J., Jaoul, O., 2003. Creep of polycrystalline anorthite and diopside. J. Geophys. Res. 108 (B1), 2061, doi:10.1029/2002JB001815.

Dimanov, A., Xiao, X., Dresen, G., Wirth, R., 1999. Grain boundary diffusion creep of synthetic anorthite aggregates: the effect of water. J. Geophys. Res. 104, 10483–10497.

Egydio-Silva, M., Vauchez, A., Bascou, J., Hippertt, J., 2002. High-temperature deformation in the Neoproterozoic transpressional Ribeira belt, southeast Brazil. Tectonophysics 352, 203–224.

Ellis, S., Stöckhert, B., 2004. Elevated stresses and creep rates beneath the brittle-ductile transition caused by seismic faulting in the upper crust. J. Geophys. Res. 109, B05407, doi:10.1029/2003JB002744.

Evans, B., 2005. Creep constitutive laws for rocks with evolving structure. In: Bruhn, D., Burlini, L. (Eds.), High-Strain Zones: Structure and Physical Properties. Geological Society, London, Special Publications, vol. 245, pp. 329–346.

Evans, A.G., Rice, J.R., Hirth, J.P., 1980. Suppression of Cavity Formation in Ceramics: Prospects for Superplasticity. J. Am. Ceram. Soc. 63, 368–375.

Farver, J.R., Yund, R.A., 1995. Interphase boundary diffusion of oxygen and potassium in K-feldspar/quartz aggregates. Geochim. Cosmochim. Acta 59, 3697–3705.

Gleason, G.C., Tullis, J., 1995. A flow law for dislocation creep of quartz aggregates determined with the molten salt cell. Tectonophysics 247, 1–23.

Godard, G., van Roermund, H.L.M., 1995. Deformation-induced clinopyroxene fabrics from eclogites. J. Struct. Geol. 17, 1425–1443.

Grevel, K.D., Chatterjee, N.D., 1992. A modified Redlich-Kwong equation of state for H2-H2O fluid mixtures at high pressures and at temperatures above 400°C. Eur. J. Mineral. 4, 1303–1310.

Hauksson, E., 2000. Crustal structure and seismicity distribution adjacent to the Pacific and North America plate boundary in southern California. J. Geophys. Res. 105 (B6), 13875–13903.

Hearn, E.H., Bürgmann, R., Reilinger, R.E., 2002. Dynamics of Izmit earthquake postseimic deformation and loading of the Düzce earthquake hypocenter. Bull. Seismol. Soc. Am. 92 (1), 172–193.

Hetland, E.A., Hager, B.H., 2003. Postseismic relaxation across the Central Nevada Seismic Belt. J. Geophys. Res. 108 (B8), 2394, doi:10.1029/2002JB002257.

Hier-Majumder, S., Mei, S., Kohlstedt, D.L., 2005. Water weakening of clinopyroxenite in diffusion creep. J. Geophys. Res. 110 (B7), B07406, doi:10.1029/2004JB003414.

Hirth, G., Teyssier, C., Dunlap, W.J., 2001. An evaluation of quartzite flow laws based on comparisons between experimentally and naturally deformed rocks. Int. J. Earth Sci. 90, 77–87.

Ingrin, J., Latrous, K., Doukhan, J.C., Doukhan, N., 1989. Water in diopside: An electron microscopy and infrared spectroscopy study. Eur. J. Mineral. 1, 327–341.

Johnson, E.A., Rossman, G.R., 2004. A survey of hydrous species and concentrations in igneous feldspars. Am. Mineral. 89, 586–600.

Karato, S., Jung, H., 2003. Effects of pressure on high-temperature dislocation creep in olivine. Philos. Mag. 83, 401–414.

Kassner, M.E., Hayes, T.A., 2003. Creep cavitation in metals. Int. J. Plast. 19 (10), 1715–1748.

Kenkmann, T., 1997. Verformungslokalisation in gabbroiden Gesteinen. Mikrostructurelle und Mineralogishe Untersuchungen in einer Hochtemperatur-Scherzone der Ivrea-Zone, Italien. Ph.D. thesis, GeoForshungs ZentrumPotsdam.

Kenkmann, T., Dresen, G., 1998. Stress gradients around porphyroclasts: paleopiezometric estimates and numerical modelling. J. Struct. Geol. 20 (2/3), 163–173.

Kenkmann, T., Dresen, G., 2002. Dislocation microstructures and phase distribution in a lower crustal shear zone – an example from the Ivrea-Zone, Italy. Int. J. Earth Sci. 91, 445–458.

Kenner, S.J., Segall, P., 2000. Postseismic deformation following the 1906 San Francisco earthquake. J. Geophys. Res. 105 (B6), 13195–13209.

Kenner, S.J., Segall, P., 2003. Lower crustal structure in northern California: implications from strain rate variations following the 1906 San Francisco earthquake. J. Geophys. Res. 108 (B1), 2011, doi:10.1029/2001JB000189.

Kim, B.N., Hiraga, K., Morita, K., Sakka, Y., 2001. A high-strain-rate superplastic ceramic. Nature 413, 288–291.

Kruse, R., Stünitz, H., 1999. Deformation mechanisms and phase distribution in mafic high-temperature mylonites from the Jotun Nappe, southern Norway. Tectonophysics 303, 223–249.

Kohlstedt, D.L., Evans, B., Mackwell, S.J., 1995. Strength of the lihosphere: Constraints imposed by laboratory experiments. J. Geophys. Res. 100 (B9), 17587–17602.

Langdon, T.G., 1995. Mechanisms of superplastic flow. In: Ridley, N. (Ed.), Superplasticity: 60 Years after Pearson. The Institute of Materials, London, pp. 9–24.

Li, V.C., Rice, J.R., 1987. Crustal deformation in great California earthquake cycles. J. Geophys. Res. 92 (B11), 11533–11551.

Mackwell, S.J., Zimmerman, M.E., Kohlstedt, D.L., 1998. High-temperature deformation of dry diabase with application to tectonics on Venus. J. Geophys. Res. 103, 975–984.

Magistrale, H., Zhou, H.W., 1996. Lithologic control of the depth of earthquakes in Southern California. Science 273 (5275), 639–642.

Mauler, A., Godard, G., Kunze, K., 2001. Crystallographic fabrics of omphacite, rutile and quartz in Vendee eclogite (Armorican Massif, France): consequences for deformation mechanisms and regimes. Tectonophysics 342, 81–112.

Mei, S., Kohlstedt, D.L., 2000a. Influence of water on plastic deformation of olivine aggregates: 1. Diffusion creep regime. J. Geophys. Res. 105, 21457–21469.

Mei, S., Kohlstedt, D.L., 2000b. Influence of water on plastic deformation of olivine aggregates: 2. Dislocation creep regime. J. Geophys. Res. 105, 21471–21481.

Montési, L.G.J., 2004. Postseismic deformation and the strength of ductile shear zones. Earth Planets Space 56, 1–7.

Nieh, T.G., Wadsworth, J., Sherby, O.D., 1997. Superplasticity in Metals and Ceramics. Cambridge University Press, Cambridge. 273p.

Olgaard, D.L., Evans, B., 1988. Grain growth in synthetic marbles with added mica and water. Contrib. Mineral. Petrol 100, 246–260.

Onck, P., van der Giessen, E., 1998. Growth of an initially sharp crack by grain boundary cavitation. J. Mech. Phys. Sol. 47, 99–139.

Özalaybay, S., Ergin, S., Aktar, M., Tapirdamaz, C., Bicmen, F., Yörük, A., 2002. The 1999 Izmit earthquake sequence in Turkey: seismological and tectonic aspects. Bull. Seismol. Soc. Am. 92 (1), 376–386.

Passchier, C.W., Trouw, R.A.J., 1996. Microtectonics. Springer Verlag, Berlin and Heidelberg, 289 pp.

Paterson, M.S., 1990. Superplasticity in geological materials. In: Mayo, M.J., Kobayashi, M., Wadsworth J. (Eds.), Superplasticity in Metals, Ceramics and Intermetallics. Material Research Society Symposium Proceedings 196. pp. 303–312.

Paterson, M.S., Olgaard, D.L., 2000. Rock deformation tests to large shear strains in torsion. J. Struct. Geol. 22, 1341–1358.

Pilling, J., Ridley, N., 1988. Cavitation in superplastic alloys and the effect of hydrostatic pressure. Res. Mech. 23, 31–63.

Post, A.D., Tullis, J., Yund, R.A., 1996. Effects of chemical environment on dislocation creep of quartzite. J. Geophys. Res. 101 (B10). 222143–22155.

Ravichandran, K.S., Seetharaman, V., 1993. Prediction of steady state creep behaviour of two phase composites. Acta Metall. Mater. 41, 3351–3361.

Riedel, H., 1993. Fracture mechanics. In: Mughrabi, H. (Ed.), Plastic deformation and fracture of materials. Mater. Sci. Technol., 6, pp. 565–628.

Rolandone, F., Bürgmann, R., Nadeau, R.M., 2004. The evolution of the seismic–aseismic transition during the earthquake cycle: constraints from the time-dependent depth distribution of aftershocks. Geophys. Res. Lett. 31, L23610, doi:10.1029/2004GL021379.

Rybacki, E., Dresen, G., 2000. Dislocation and diffusion creep of synthetic anorthite aggregates. J. Geophys. Res. 105 (B11), 26017–26036.

Rybacki, E., Paterson, M.P., Wirth, R., Dresen, G., 2003. Rheology of calcite-quartz aggregates deformed to large strain in torsion. J. Geophys. Res. 108 (B2), 2089, doi:10.1029/2002JB001833.

Rybacki, E., Dresen, G., 2004. Deformation mechanism maps for feldspar rocks. Tectonophysics 382 (3–4), 173–187.

Rybacki, E., Gottschalk, M., Dresen, G., 2004. Effect of water fugacity on creep strength of anorthite. Eos Trans. AGU Fall Meet. Suppl. 85 (47). T41B–1178 (Abstract).

Rybacki, E., Gottschalk, M., Wirth, R., Dresen, G., 2006. Influence of water fugacity and activation volume on the flow properties of fine-grained anorthite aggregates. J. Geophys. Res. 111, B03203, doi:10.1029/2005JB003663.

Savage, J.C., 2000. Viscoelastic-coupling model for the earthquake cycle driven from below. J. Geophys. Res. 105 (B11), 25525–25532.

Savage, J.C., Svarc, J.L., 1997. Postseismic deformation associated with the 1992 Mw = 7.3 Landers earthquake, southern California. J. Geophys. Res. 102 (B 4), 7565–7577.

Savage, J.C., Svarc, J.L., Prescott, W.H., 2003. Near-field postseismic deformation associated with the 1992 Landers and 1999 Hector Mine, California, earthquakes. J. Geophys. Res. 108 (B9), 2432, doi:10.1029/2002JB002330.

Scholz, C., 1990. The mechanics of earthquakes and faulting. Cambridge University Press, New York.

Sibson, R., 1977. Faults rocks and fault mechanisms. J. Geol. Soc. London 133, 191–213.

Skogby, H., Rossman, G.R., 1989. OH in pyroxene: An experimental study of incorporation mechanisms and stability. Am. Mineral. 74, 1059–1069.

Steffen, K., Selverstone, J., Brearley, A., 2001. Episodic weakening and strengthening during synmetamorphic deformation in a deep-crustal shear zone in the Alps. In: Holdsworth, R.E., Strachan, R.A., Magloughlin, J.F., Knipe, R.J. (Eds.), The Nature and Tectonic Significance of Fault Zone Weakening. Geological Society, London, Special Publications, vol. 186, pp. 141–156.

Tekeli, S., 2002. Cavity Formation During High Temperature Deformation in 3YTZP/Al_2O_3 composites containing 20 to 60 wt% Al_2O_3. Mater. Sci. Technol. 18, 87–91.

Thatcher, W., 1983. Nonlinear strain buildup and the earthquake cycle on the San Andreas fault. J. Geophys. Res. 88, 5893–5902.

Tibi, R., Bock, G., Xia, Y., Baumbach, M., Grosser, H., Milkereit, C., Karakisa, S., Zünbül, S., Kind, R., Zschau, J., 2001. Rupture process of the 1999 August 17 Izmit and November 12 Düzce (Tukey) earthquakes. Geophys. J. Int. 144, F1–F7.

Trepmann, C.A., Stöckhert, B., 2003. Quartz microstructures developed during non-steady state plastic flow at rapidly decaying stress and strain rate. J. Struct. Geol. 25 (12), 2035–2051.

Tse, S., Rice, J., 1986. Crustal earthquake instability in relation to the depth variation of frictional slip properties. J. Geophys. Res. 91, 9452–9472.

Tullis, T.E., Horowitz, F.G., Tullis, J, 1991. Flow laws of polyphase aggregates from end-member flow laws. J. Geophys. Res. 96 (B5), 8081–8096.

Vetrano, J.S., Simonen, E.P., Bruemmer, S.M., 1999. Evidence for excess vacancies at sliding grain boundaries during superplastic deformation. Acta Mater. 47, 4125–4129.

Wakai, F., Kondo, N., Shinoda, Y., 1999. Ceramics superplasticity. Curr. Opin. Solid State Mater. Sci. 4, 461–465.

Wang, Z., Dresen, G., Wirth, R., 1996. Diffusion creep of fine-grained polycrystalline anorthite at high temperature. Geophys. Res. Lett. 23, 3111–3114.

Wheeler, J., 1992. Importance of pressure solution and Coble creep in the deformation of polymineralic rocks. J. Geophys. Res. 94 (B4), 4579–4586.

White, J., White, S., 1983. Semi-brittle deformation within the Alpine fault zone. N.Z.J. Struct. Geol. 5, 579–589.

Wilkins, R.W.T., Sabine, W., 1973. Water content of some nominally anhydrous silicates. Am. Mineral. 58, 508–516.

Yoon, C.K., Chen, I.W., 1990. Superplastic flow of two-phase ceramics containing rigid inclusions – zirconia/mullite composites. J. Am. Ceram. Soc. 73, 1555–1565.

Zelin, M.G., Mukherjee, A.K., 1996. Geometrical aspects of superplastic flow. Mater. Sci. Eng. A208, 210–225.

Zener, C., 1948. The micro-mechanism of fracture. In: Johnson, F., Roop, W.P., Bayles, R.T. (Eds.), Fracturing of Metals. ASM, Cleveland, pp. 3–31.